The Creation of Algorithms Designed for Analyzing Periodic Surfaces of Crystals and Mineralogically Important Sites in Molecular Models of Crystals:

Understanding the Electron Density Function Through Visual Examinations of the Curvature and Shape of the Equi-Value Laplacian Surfaces

Lesa L. Beverly

Dissertation submitted to the Faculty of the
Virginia Polytechnic Institute and State University
in partial fulfillment of the requirements for the degree of

Doctor of Philosophy
in
Mathematics

Monte B. Boisen, Jr., Chair
Ezra Brown
Gerald V. Gibbs
Peter Haskell
Robert Rogers

July 21, 2000
Blacksburg, Virginia

Keywords: Electron Density Function, Laplacian, Surface Approximations, VRML, Disiloxane

The Creation of Algorithms Designed for Analyzing Periodic Surfaces of Crystals and Mineralogically Important Sites in Molecular Models of Crystals:

Understanding the Electron Density Function Through Visual Examinations of the Curvature and Shape of the Equi-Value Laplacian Surfaces

Lesa L. Beverly

(ABSTRACT)

The goals of the research presented in this dissertation were to create algorithms that produce images of complex phenomena, to study the efficacy of the algorithms, and to apply these algorithms to important mineralogical problems. The algorithms that were created include the Sphere Projection method, the Chicken Wire method, and methods for calculating the curvature at any point on a surface. The Sphere Projection method is best applied to roughly spherical surfaces. A theorem about the "fit" to a sphere determines the accuracy of the model in this special case and gives some insight into the limitations of this method. The Chicken Wire method was developed to model those surfaces for which the Sphere Projection method was ineffective. The effectiveness of the Chicken Wire method was also determined.

The algorithms were used to produce images of equi-value surfaces of the Laplacian of the electron density function in selected molecules. The water molecule, H_2O, was studied to demonstrate that these new methods are capable of reproducing known features. The disiloxane molecule, $H_6Si_2O_7$, was studied because it serves as a model for bonding in quartz and other important silicates. Lastly, the molecule $NaLi_2Si_2OF_9$ was examined as a molecular model for low albite. A new discovery suggests that these algorithms will be an important tool in mineralogy.

NSF is generously thanked for supporting this study with grant #EAR-9627458.

Dedication

To Chris,

I couldn't have done it without you.

Acknowledgments

To the Virginia Tech Math Department, I want to express my appreciation for the support that you have shown to me. Your kindness to my family after my son's accident was exceptional. I feel truly blessed to have shared the past six years with you. Thank you for helping me grow as a mathematician, as a teacher, and as an individual.

To Eileen Shugart, you are a wonderful person. Thank you for sharing your teaching skills with me and every other graduate student in the department. Your patience in inexhaustible. It is, however, the friendship that developed between us for which I am most thankful. Your prayers, love, and support has been a tremendous help to me over the past years.

To Chris Massey, I owe you a lot. You helped me in so many ways this past year. I am very thankful for all your help and, most of all, for your friendship.

To Dr. G.V. Gibbs, thank you for the all the help with my research. I look forward to continued collaboration.

To Dr. Monte B. Boisen, Jr., I don't even know where to begin to thank you for your guidance. Thank you for tolerating the constant knocks on your door. Thank you for taking the time to instill confidence as well as knowledge. Thank you for helping me to grow as a teacher as well as a mathematician. Thank you for worrying about me. Most of all, thank you for sharing your friendship.

To my best friends, Lisa Stanley, Dawn Stewart, and Kevin Hulsing, I miss you all. I am very thankful for the gift of your friendship. Without you, this project would have been so much more difficult. Thank you for the reminders to take a deep breath. Thank you for the daily encouragement while you were at VT and the email encouragement when you were not. Thank you for the ice cream and cheesecake retreats when things became a little to hectic. I love you all and wish you the best in all you do. You're the greatest!

To my mom and dad, I love you both so much. I feel extremely lucky to have been born your daughter. Thank you for your love and support.

To my second mom, thank you so much for treating me not as a daughter-in-law, but as a daughter.

To my second dad, I miss you. I know that you have been with me each and every step of

the way though and that you are smiling down at me from Heaven. Thank you for loving me as one of your own.

To my children, Shawn and Ashley, I am so thankful for both of you. It is because of you that I decided to pursue my doctorate. I wanted you to see that you should always go after you dreams, no matter how far-fetched they may seem. Thank you for putting up with me for the past few years. I know I wasn't always the nicest mom to come home to or to have come home to you. I am however the mom that loves you more than life itself.

Finally, to my husband, Chris, I have so much to say but don't know where to start. Thank you so much for your faith in me. You saw beyond my fears and recognized my need and desire to pursue this degree. You put those same needs and desires ahead of your own, making you the most special person in the world. Thank you for pushing me when I needed pushed, for letting me cry when I was frustrated, for carrying me when I was tired, for encouraging me at the first sign that I was losing faith, for celebrating with me the smallest accomplishment. You are an amazing man and I love you.

Contents

1 Introduction **1**

2 The Electron Density Function and Its Laplacian **4**

2.1 The Electronic Problem 4

2.1.1 Schrödinger's Equation 4

2.1.2 The Born-Oppenheimer Approximation 6

2.1.3 Molecular Orbitals 7

2.2 Electron Density Function 10

3 Using the Sphere Projection Method to Model Surfaces **11**

3.1 Triangulation of the Sphere 12

3.2 The Sphere Triangulation: How Accurate Is It? 14

3.3 Projection of the Sphere onto the Desired Surface 16

3.4 Modeling the Zero Laplacian Surfaces of H_2O 17

4 Using the Chicken Wire Method to Model Surfaces **20**

4.1 The Triangulation of the Hexagon 20

4.2 Finding the starting vectors for the hexagonal system 24

4.3 Creating the First and Second Hexagonal Rings 25

4.4 How do you find a general point on the surface? 26

4.5 The Algorithm for Growing the Hexagonal Net 27

4.6 The Chicken Wire Method: How Accurate Is It? 28

4.7 Applications 30

5 Curvature **32**

5.1 Computation of Orthogonal Basis 33

5.2 Computation of the Hessian 34

5.3 Applications to the Study of Mineralogy 34

6 Applications to the Laplacian **38**

6.1 Application to Water 41

6.2 Application to $H_6Si_2O_7$ 43

6.3 Application to $NaLi_2Si_2OF_9$ 48

7 Future Work **50**

List of Figures

3.1 2-D image of the Zero Laplacian surfaces of water. 11

3.2 Spheres triangulated from 86, 188, 1322, and 31,860 points, respectively. . . 16

3.3 Middle zero Laplacian shell of water. 18

3.4 Outer zero Laplacian shell of water. 19

3.5 Example of a problem with the Sphere Projection method on the water molecule. 19

4.1 Hexagonal ring pattern. 21

4.2 Triangulating the hexagonal rings. 21

4.3 Labeling the triangulation vertices. 22

4.4 Chicken wire 24

4.5 3D representation $-\nabla^2\rho(\mathbf{r}) = 19$ of $NaLi_2Si_2OF_9$ 31

4.6 3D representation $-\nabla^2\rho(\mathbf{r}) = 19$ sliced through the SiOSi plane and a plane perpendicular to the SiOSi plane of $NaLi_2Si_2OF_9$ 31

5.1 3-Dim representations of the Zero Laplacian isosurface of $NaLi_2Si_2OF_9$ . . . 35

5.2 3-Dim representations of the -19 Laplacian isosurface of $NaLi_2Si_2OF_9$. . . . 35

5.3 3-Dim representations of the -19 Laplacian isosurface and the Zero Laplacian isosurface of $NaLi_2Si_2OF_9$ graphed together. 36

5.4 3-Dim representations of the Zero Laplacian isosurface of $H_6Si_2O_7$ 36

5.5 3-Dim representations of the -15 Laplacian isosurface of $H_6Si_2O_7$. 37

5.6 3-Dim representations of the -15 Laplacian isosurface and the Zero Laplacian isosurface of $H_6Si_2O_7$ graphed together. 37

6.1 Relief maps of the total charge density and the Laplacian for the water molecule in the plane $\perp$ to HOH plane. Images taken from MacDougall [17]. . . 39

6.2 Relief maps of the total charge density and the Laplacian for the water molecule in the HOH plane. Images taken from MacDougall [17]. 40

6.3 3D representation of the $-\nabla^2\rho(\mathbf{r})$ surface of the water molecule. 42

6.4 Ball and stick model of $H_6Si_2O_7$. 43

6.5 3D representation $-\nabla^2\rho(\mathbf{r})$ of $H_6Si_2O_7$ (SiOSi plane). 44

6.6 3D representation $-\nabla^2\rho(\mathbf{r})$ of $H_6Si_2O_7$ (plane $\perp$ to SiOSi plane). 45

6.7 3D representation $-\nabla^2\rho(\mathbf{r})$ of $H_6Si_2O_7$ (SiOH plane). 47

6.8 3D representation $-\nabla^2\rho(\mathbf{r})$ of $H_6Si_2O_7$ (plane $\perp$ to SiOH plane). 47

6.9 3D representation $-\nabla^2\rho(\mathbf{r})$ of $NaLi_2Si_2OF_9$ sliced through the SiOSi plane. 48

6.10 3D representation $-\nabla^2\rho(\mathbf{r})$ of $NaLi_2Si_2OF_9$ sliced through a plane perpendicular to the SiOSi plane. 49

Chapter 1

Introduction

Much time and deliberation went into the search for the subject of this dissertation. The topic should not simply be a problem to be solved, published, and forgotten, but one that would open the door to future research projects. The area would be mathematical crystallography but the contribution to be made to the field was not nearly as obvious.

In March, 1998, the Center for Discrete Mathematics and Theoretical Computer Science (DIMACS) at Rutgers University hosted the DIMACS Workshop on Discrete Mathematical Chemistry. Many of the experts in the field were present and eager to share ideas and information. In particular, the author became intrigued by the work of Andreas Dress from the Universitat Bielefeld in Germany, Stephen T. Hyde from the Australian National University, and P.G. Mezey from the University of Saskatchewan, Canada. Each of these researchers was studying molecular and crystalline geometry in very different ways.

Dr. Dress' talk was entitled "Constructive Molecular Geometry". His students were also presenters and their work followed a similar path. Gunnar Brinkman (Bielefeld) discussed "Problems in Generating Chemical Structures" and David Huson (Princeton University) presented "The Combinatorics of Periodic Tilings" in which periodic three-dimensional tilings were classified and possible applications to the enumeration of crystal structures were

discussed.

Dr. Hyde presented his work on "2-d Hyperbolic Nets". He claimed that many "chemically relevant frameworks can be mapped onto the simpler low genus three-periodic hyperbolic surfaces, related to the three-periodic minimal surfaces" [15]. This implies that the ball and stick models of some crystals can be analyzed in a two dimensional hyperbolic geometrical setting. Hyde uses the idea of curvature to explain some of his theories. Further correspondence with Hyde introduced the author to the three-dimensional visualization tool, VRML, Virtual Reality Modeling Language. Curvature and VRML have played a significant role in the work presented in this dissertation.

Dr. Mezey's work was closest to the interests of the author and her advisor. His presentation was entitled "Topological Methods of Molecular Shape Analysis". In this work and in other work, Dr. Mezey discusses the role of the electron density function in the quest for more information on chemical reactivity and chemical interactions [1]. The work done by Boisen and Gibbs also supports the importance of the electron density function. In particular, research by Boisen, Gibbs, Bader, MacDougall, and others demonstrates that it is the Laplacian of the electron density function that has the capability to reveal interesting properties of molecular and crystalline structures [8, 12, 11, 13, 10, 5, 6, 4, 17].

As a result of the exposure to the research described here, the topic of this dissertation became focused on creating algorithms and subsequent software that would be capable of using shape analysis and curvature to study the Laplacian of the electron density function. Such tools would provide a means of gathering data that might lead to insights into the electronic properties of atoms in molecular models of crystals. Knowledge of bonding interactions and reaction mechanisms within a molecular or crystal structure is crucial to the understanding of crystal chemistry, phase transformations, weathering, bacterial attack, and many other geochemical processes.

The idea of constructing tools that would make it possible to visually examine the isosurfaces of the Laplacian of the electron density distribution quickly followed from the idea of using shape analysis as a tool to study molecular models. "You have to **see** it before you can **think** it" has become the motto of this project. This means that before a scientist can find a new phenomenon, he has to be given a reason to look for it. Creating faithful images of the isosurfaces allows for the visual inspection of something that could not be seen with the naked eye or even with two dimensional images, and hence for the discovery of the existence of something that had gone previously unidentified. This is the situation that has resulted from the algorithms that are presented in this dissertation.

The next chapter is devoted to a review of the theory of the electron density function and its Laplacian. A brief theoretical background is included to aid in the understanding of the definition of the electron density function. Because the applications of the algorithms that have been developed in this thesis deal primarily with the Laplacian of the electron density function, such an introduction is indeed necessary.

Chapter 3 introduces the algorithm that defines the Sphere Projection method. This method allows for the three-dimensional representation of a function that defines a surface that is closed and nearly convex. Because this method will not model general surface types, a second method is introduced in chapter 4. The Chicken Wire method results from the implementation of an algorithm that is capable of obtaining a three-dimensional representation of a function's isosurfaces regardless of the shape of the smooth surface. Chapter 5 discusses the algorithm that was created to calculate the curvature value for any point on a surface. Chapter 6 will present applications of the Sphere Projection method and Chicken Wire method to the molecular models of water (H_2O), the disiloxane molecule, ($H_6Si_2O_7$), and the molecule $NaLi_2Si_2OF_9$. Finally, chapter 7 will discuss the possible directions for future research for the author.

Chapter 2

The Electron Density Function and Its Laplacian

This chapter is devoted to providing a brief sketch of the theoretical background of the electron density function and its Laplacian. The electron density function is a function from 3-space to the reals, as is its Laplacian. In this dissertation, the level curves (called isosurfaces) of the Laplacian of the electron density function are of primary interest. Before the electron density function can be defined, however, it is necessary to define the elements of which it is composed. The material which comprises this chapter is contained in classical quantum mechanics books such as those written by Szabo and Ostlund [21], McWeeny [18], Pople [19], and Ashcroft and Mermin [2].

2.1 The Electronic Problem

2.1.1 Schrödinger's Equation

Describing the motions of electrons in the field of nuclear point charges is a problem at the heart of quantum chemistry. Solving this problem requires that a solution be found to the

Schrödinger partial differential equation

$$\hat{H}\Psi = E\Psi \quad . \tag{2.1}$$

$\hat{H}$ denotes the Hamiltonian, a differential operator representing the total energy. $\hat{H}$ is composed of a kinetic energy part and a potential energy part.

$$\hat{H} = \hat{T} + \hat{V} \tag{2.2}$$

$\hat{T}$ denotes the kinetic energy part and is defined to be

$$\hat{T} = -\frac{\hbar^2}{8\pi^2} \sum_i \frac{1}{m_i} \left(\frac{\partial^2}{\partial x_i^2} + \frac{\partial^2}{\partial y_i^2} + \frac{\partial^2}{\partial z_i^2} \right) \tag{2.3}$$

with i signifying summation over all particles (nuclei and electrons), m_i representing the mass of the ith particle, and $\hbar$ being Planck's constant. $\hat{V}$ denotes the coulomb potential energy part defined by

$$\hat{V} = \sum_i \sum_{j \neq i} \left(\frac{e_i e_j}{r_{ij}} \right) \tag{2.4}$$

with the sums over distinct pairs of particles (i,j) separated by distance r_{ij} with charges e_i and e_j.

E denotes the numerical value of the energy relative to a state in which the nuclei and electrons are infinitely separated and at rest. Ψ is the wave function that is dependent on the Cartesian coordinates of all particles as well as on the spin coordinates of the particles. $|\Psi|^2$ is the measure of the probability distribution on the particles within the molecule. One restriction must be imposed on the wave functions to make a solution to equation (2.1) physically acceptable. This is referred to as the *Anti-Symmetric Principle* which states that a many-electron wave function must be anti-symmetric with respect to the interchange of the coordinates $\mathbf{x}$ of any two electrons, i.e.

$$\Psi(\mathbf{x}_1, \ldots, \mathbf{x}_i, \ldots, \mathbf{x}_j, \ldots, \mathbf{x}_N) = -\Psi(\mathbf{x}_1, \ldots, \mathbf{x}_j, \ldots, \mathbf{x}_i, \ldots, \mathbf{x}_N) \quad . \tag{2.5}$$

Here $\mathbf{x} = \{\mathbf{r}, \omega\}$ where $\mathbf{r}$ represents the position coordinates and ω represents the spin coordinates.

2.1.2 The Born-Oppenheimer Approximation

To simplify the general molecular problem in quantum mechanics, the Born-Oppenheimer Approximation was developed. This method allowed the electronic calculations to be separated from the those of the nuclei. Nuclear masses are much greater than those of the electrons and thus the nuclei move much more slowly than the electrons. Hence, as long as the ratio of electrons to the nuclear mass is sufficiently small, it is reasonable to suppose that the electron distribution is dependent only on the instantaneous positions of the nuclei and not on their velocities. In other words, the positions of the nuclei can be assumed to be fixed. This creates an effective electronic energy, denoted $E^{eff}(R)$, which is dependent on the relative nuclear coordinates, R. E^{eff} is then used in place of the potential energy contribution.

Equation (2.1) now can be restated solely in terms of the electronic contribution as

$$\hat{H}^{elec}\Psi^{elec}(r, R) = E^{eff}(R)\Psi^{elec}(\mathbf{r}, R) \tag{2.6}$$

Ψ^{elec} is the electronic wave function that is dependent on the electronic coordinates, $\mathbf{r}$, as well as on R. $\hat{H}^{elec}$ is the Hamiltonian modified so that only the electronic energy is calculated. It is defined as

$$\hat{H}^{elec} = \hat{T}^{elec} + \hat{V} \tag{2.7}$$

with $\hat{T}^{elec}$ defined as before with the exception that the sum is now only over the electrons.

The goal of many of the theoretical studies of electronic structures is to solve the electronic Schrödinger equation (equation (2.1)) and thus to find an effective nuclear potential

function, E^{eff}. Henceforth, the superscripts will be dropped and it will be assumed that $\hat{H}$, Ψ, and E refer to electronic motion only.

$E(R)$ is fundamental to the quantitative description of chemical structures and reaction processes. The lowest energy solution is the ground-state potential energy surface. There will generally be a number of local minima which corresponds to the geometry that a molecule would have if the nuclei were stationary. There may also exist saddle points, stationary points where there are one or more orthogonal directions. In at least one of those directions, the energy is a maximum and in another, a minimum. This corresponds to a transition structure for chemical reactions.

2.1.3 Molecular Orbitals

This section will be devoted to the wave functions. In particular, the approximation of wave functions will be discussed. In practice, wave functions are approximated by one-electron functions often called *orbitals*. Molecular orbitals are denoted by $\psi(x, y, z)$ where (x, y, z) is the Cartesian coordinates of one electron. $|\psi|^2$ is the probability distribution of the electron in space.

The approximation to a full wave function must also include a spin component. There are two possible values for the spin component, $\frac{1}{2}$ and $-\frac{1}{2}$. These values measure the spin angular momentum along the z-axis. A spin in the direction of the positive z-axis is denoted by $\alpha(\xi)$ with $\alpha(\frac{1}{2}) = 1$ and $\alpha(-\frac{1}{2}) = 0$. Similarly, a spin in the direction of the negative z-axis is denoted by $\beta(\xi)$ with $\beta(\frac{1}{2}) = 0$ and $\beta(-\frac{1}{2}) = 1$.

The complete wave function for a single electron is then the product of the molecular orbitals and their corresponding spin functions, i.e.

$$\psi(x, y, z)\alpha(\xi) \qquad \text{or} \qquad \psi(x, y, z)\beta(\xi). \tag{2.8}$$

This will be called the *s*pin orbital and denoted $\Upsilon(x, y, z, \xi)$. To ensure that the anti-symmetry principle is upheld, the spin orbitals may be arranged in a determinantal wave function

$$\Psi_{determinant} = \begin{vmatrix} \Upsilon_1(1) & \Upsilon_2(1) & \dots & \Upsilon_n(1) \\ \Upsilon_1(2) & \Upsilon_2(2) & \dots & \Upsilon_n(2) \\ \vdots & \vdots & \ddots & \vdots \\ \Upsilon_1(n) & \Upsilon_2(n) & \dots & \Upsilon_n(n) \end{vmatrix} \tag{2.9}$$

This can be expanded and written in the form

$$\Psi_{determinant} = \sum_P (-1)^P \hat{P} \left[\Upsilon_1(1), \Upsilon_2(2), \dots, \Upsilon_n(n)\right] \tag{2.10}$$

where $\hat{P}$=permutation operator on the coordinates and $(-1)^P = 1$ or -1 depending on whether $\hat{P}$ is an even or odd permutation, respectively. Note that it is not possible for two electrons of the same spin to occupy the same orbital. If so, two columns of $\Psi_{determinant}$ would be identical and consequently $\Psi_{determinant}$ would vanish. Thus the anti-symmetry principle (also called the *Pauli-Exclusion Principle*) is upheld.

The molecular orbitals have the property that they are orthogonal to each other, i.e.

$$S_{ij} = \int \psi_i^* \psi_j \mathrm{d}x\mathrm{d}y\mathrm{d}z = 0 \quad \text{for } i \neq j.$$

The spin components are also orthogonal by integration over spin space which is simply the summation over the two possible values of ξ, i.e.

$$\sum_\xi \alpha(\xi)\beta(\xi) = \alpha(\frac{1}{2})\beta(\frac{1}{2}) + \alpha(-\frac{1}{2})\beta(-\frac{1}{2}) = 0.$$

Molecular orbitals may be normalized by multiplying ψ_i by a constant,

$$S_{ii} = \int \psi_i^* \psi_i \mathrm{d}x\mathrm{d}y\mathrm{d}z = 1.$$

Then the wave function can similarly be normalized so that

$$\int \cdots \int \Psi^* \Psi \mathrm{d}\tau_1 \ldots \mathrm{d}\tau_n = 1.$$

By applying the above properties, the full many-electron molecular orbital wave function for a closed-shell ground state of a molecule with n (even) electrons, doubly occupying $\frac{n}{2}$ orbitals can be written as

$$\Psi = (n!)^{-\frac{1}{2}} \begin{vmatrix} \psi_1(1)\alpha(1) & \psi_1(1)\beta(1) & \psi_2(1)\alpha(1) & \ldots & \psi_{\frac{n}{2}}(1)\beta(1) \\ \psi_1(2)\alpha(2) & \psi_1(2)\beta(2) & \psi_2(2)\alpha(2) & \ldots & \psi_{\frac{n}{2}}(2)\beta(2) \\ \vdots & \vdots & \vdots & \ddots & \vdots \\ \psi_1(n)\alpha(n) & \psi_1(n)\beta(n) & \psi_2(n)\alpha(n) & \ldots & \psi_{\frac{n}{2}}(n)\beta(n) \end{vmatrix}.$$

This form of Ψ is called the *Slater determinant.*

Basis Expansion of Molecular Orbitals

The last section explains how many electron wave functions are composed from molecular orbitals. In practice, a restriction is also imposed that requires that each molecular orbital be expressed as a linear combination of a finite set of N prescribed one-electron functions. This set of functions are called the *basis functions.* Thus each molecular orbital, ψ_i, can be written as

$$\psi_i = \sum_{\mu}^{N} c_{\mu i} \phi_\mu$$

where $\phi_1, \phi_2, \ldots, \phi_N$ are the basis functions and the $c_{\mu i}$ are molecular orbital expansion coefficients. According to Ashcroft and Mermin [2], this restriction reduces the problem of finding complete descriptions of the three-dimensional function ψ_i to finding only a finite set of linear coefficients for each orbital.

2.2 Electron Density Function

Now that the necessary background material has been provided, the *electron density function* can be defined. The electron density function (also called the electron probability distribution function), denoted $\rho(r)$, is a three-dimensional function defined as

$$\rho(r) = \sum_{\mu}^{N} \sum_{\nu}^{N} P_{\mu\nu} \phi_{\mu} \phi_{\nu} \tag{2.11}$$

where the ϕ's are the basis functions described in the previous section and $P_{\mu\nu}$ is the density matrix defined as

$$P_{\mu\nu} = 2 \sum_{i=1}^{occ} c_{\mu i}^{*} c_{\nu i}. \tag{2.12}$$

The sum is over the occupied molecular orbitals only and the $c_{\mu i}$ and $c_{\nu i}$ represent the corresponding molecular orbital expansion coefficients described in the previous section.

The Laplacian of the electron density function, denoted $\nabla^2 \rho(r)$, is then defined to be

$$\nabla^2 \rho(r) = \frac{\partial^2 \rho(r)}{\partial x^2} + \frac{\partial^2 \rho(r)}{\partial y^2} + \frac{\partial^2 \rho(r)}{\partial z^2} \quad . \tag{2.13}$$

The electron density function and its Laplacian have become major players in the quest for insight into molecular and crystal structure and reaction mechanism. More information about this role will be given in Chapter 6.

Chapter 3

Using the Sphere Projection Method to Model Surfaces

The Laplacian of the Electron Density function is often represented by clearly defined concentric shells. Initial studies of these shells led to an interest in the Zero Laplacian surfaces, i.e. those surfaces satisfying $\nabla^2\rho(r) = 0$. These surfaces are often closed and sometimes convex. As an example, Figure(3.1) is a two dimensional image of the Zero Laplacian surfaces of the water molecule created through the implementation of Fortran code supplied by Bader [3]. The resulting data was then viewed using the software package Surfer [16]. The two inner surfaces appear to be both closed and convex while the outer is only closed. Creating algorithms capable of representing both surface types in a three-dimensional format was the ultimate goal. Initial work, however, focused on the closed and convex surface type.

Figure 3.1: 2-D image of the Zero Laplacian surfaces of water.

To accomplish this task, an algorithm to project a triangulated sphere onto the desired surface was created. By using a triangulated sphere, the projection of each vertex of each triangle marks the corresponding point on the surface. After the projection of the entire sphere is complete, a record exists that gives a list of the points on the surface along with a record of what three points should be linked together to form a triangle. Thus each triangle on the sphere corresponds to a triangle on the surface.

3.1 Triangulation of the Sphere

Initial ideas of how to triangulate the sphere came out of the author's discussions with Monte B. Boisen, Jr., Kevin Dent, and Sanjiv Parikh during preparation for Mr. Dent's Master's presentation that was given at Virginia Tech in August, 1999. An algorithm and subsequent program was written by Mr. Parikh which implemented this idea. Because the author needed a more flexible program and did not have access to the source code for Parikh's program, it became necessary for the author to independently create a second algorithm and program for triangulating the sphere. The process used to create this will now be discussed.

The triangulation process uses a given value of $\epsilon \in (0, 1)$. In the final triangulation, no triangle will have a side that is larger than ϵ. All calculations are done in spherical coordinates. Let

$$LAT = \left\lceil \frac{3\pi}{4\epsilon} \right\rceil \quad .$$

Then there is an integral number $(2 * LAT - 1)$ of latitudinal lines on the sphere. Hence,the actual angle value that is being used to create the latitudinal lines is

$$\phi_0 = \frac{\pi}{2 * LAT} \qquad .$$

Now it is necessary to determine the points that will form the vertices of the triangles. This is done by determining the number and position of the points on each of the latitudinal

lines. The upper hemisphere is made up of LAT latitudinal lines . The first latitudinal line is simply the North Pole, i.e. the point $[0, 0, 1]$. Call the second latitudinal line L_2. The circumference of the circle formed by L_2 is $2\pi * \sin 2\phi_0$. So to find the number of points (N) on this circle, let

$$N = \left\lceil \frac{2\pi * \sin 2\phi_0}{\phi_0} \right\rceil \quad .$$

Then let $\theta_0 = \frac{2\pi}{N}$ which is the true arc length between the points on our circle. This process is repeated for each of the latitudinal lines on the sphere. The algorithm for determining the x, y, z values for the points on each circle follows.

Calculate LAT.
For I=1 to LAT (upper hemisphere)

Calculate N.
For J=0 to N-1

Let $\phi = \phi_0 * I$.
Let $\theta = \theta_0 * J$.
$x = \sin\phi * \cos\theta$.
$y = \sin\phi * \sin\theta$.
$z = \cos\phi$.

For II=LAT-1 to 1 (lower hemisphere)

Calculate N.
For JJ=0 to N-1

Let $\phi = \phi_0 * II$.
Let $\theta = \theta_0 * JJ$.
$x = \sin\phi * \cos\theta$.
$y = \sin\phi * \sin\theta$.
$z = -\cos\phi$.

As each step in this process is finished, the points on each latitudinal line are recorded in an ordered manner. These points will become the vertices of the triangulation and will be the points used in the projection. Each point will correspond to a point on the surface. First, however, the triangulation of these points must be completed.

Let l and m be adjacent latitudinal lines whose points are in the vectors L and M, respectively; i.e. the first point on l is $L(1)$, the second in $L(2)$, and so forth. Let k_l and k_m represent the respective number of points on l and m. To ease the description, assume that l and m are in the upper hemisphere with l closer to the North Pole. This means that $k_l \leq k_m$. (If l and m are in the lower hemisphere, switch the order of L and M in the algorithm.) The algorithm to compute the triangulation is as follows:

> Set i=1 and j=1. Let ii=i+1 and jj=j+1. If $ii > k_l$, then let $ii = 1$ and if $jj > k_m$, let $jj = 1$. Let $d(a, b)$ be the distance between the points a and b. Compute $D_1 = d\,(M(i), L(jj))$ and $D_2 = d\,(M(ii), L(j))$. If $D_1 \leq D_2$ then form the triangle with vertices $\{L(i), M(j), L(ii)\}$ and let $i = i+1$. If $i > k_l$, set $i = 1$ and set $icount = 1$. Otherwise form the triangle with vertices $\{L(i), M(j), M(jj)\}$ and let $j = j + 1$. If $j = k_m$, set $j = 1$ and set $jcount = 1$. If $icount = 1$ and $jcount = 1$, then the area has been successfully triangulated.

3.2 The Sphere Triangulation: How Accurate Is It?

Clearly there is some deviation from the surface with each triangle since the sphere is curved and the triangle is flat. The theorem below will address the accuracy of the method.

The term deviation must first be defined. There are, of course, many ways to define the area of the sphere that is being represented by a given triangle. In this theorem, the area of the sphere that is being represented by ΔABC is that area of the sphere which is hit by the normal vectors to the plane containing ΔABC that also pass through a point on or within the boundary of ΔABC. To say that a point on the triangle deviates from the surface of the sphere by a value d means that the distance from the point P on the triangle to point S, the point on the sphere which is pierced by the normal through P, is d. This definition then leads to the following theorem.

Theorem 1. *Given an equilateral triangle, ΔABC, with sides of length ϵ whose vertices, $\{A, B, C\}$, lie on the sphere $x^2+y^2+z^2 = r^2$, each point on ΔABC deviates from the surface of the sphere by at most*

$$r - \sqrt{r^2 - \frac{1}{3}\epsilon^2} \quad .$$

Proof. Let ΔABC an equilateral triangle with sides of length ϵ. Also assume that the vertices, $\{A, B, C\}$, lie on the sphere $x^2 + y^2 + z^2 = r^2$. Without loss of generality, assume

$$A = (r, 0, 0)$$

$$B = \left(r - \frac{\epsilon^2}{2r}, \frac{\epsilon}{2r}\sqrt{4r^2 - \epsilon^2}, 0 \right) \quad \text{and}$$

$$C = \left(r - \frac{\epsilon^2}{2r}, \frac{1}{\sqrt{4r^2 - \epsilon^2}} \left(\epsilon r - \frac{\epsilon^3}{2r} \right), \epsilon \sqrt{\frac{3r^2 - \epsilon^2}{4r^2 - \epsilon^2}} \right).$$

Verification that these values actually satisfy the given hypotheses can be accomplished through application of the distance formula. Further calculations show that the median of ΔABC is located at the point

$$M = \left(r - \frac{\epsilon^2}{2r}, \frac{3r^2\epsilon - \epsilon^3}{3r\sqrt{4r^2 - \epsilon^2}}, \frac{\epsilon}{3}\sqrt{\frac{3r^2 - \epsilon^2}{4r^2 - \epsilon^2}} \right) \quad .$$

Let ϑ represent the origin of the sphere. In this case, $\vartheta = (0, 0, 0)$. Note that $\overrightarrow{\vartheta M}$, the line through ϑ and M, is orthogonal to the plane with contains ΔABC since $\overrightarrow{\vartheta M} \bullet \overrightarrow{AB} = 0$, $\overrightarrow{\vartheta M} \bullet \overrightarrow{AC} = 0$, and $\overrightarrow{\vartheta M} \bullet \overrightarrow{BC} = 0$. Since $\overrightarrow{\vartheta M}$ is also perpendicular to the plane that is tangent to the sphere and that also contains the point where $\overrightarrow{\vartheta M}$ intersects with the sphere, the point on the triangle which has the greatest deviation from the surface of the sphere is M. Thus the deviation value of M is an upper bound for all the points on the triangle.

Shift the plane that contains the triangle ΔABC so that the point M is now at the origin. The vertices are now located at the points

$$\left(\frac{\sqrt{3}}{3}\epsilon, 0 \right), \quad \left(-\frac{\sqrt{3}}{6}\epsilon, \frac{\epsilon}{2} \right), \quad \text{and} \quad \left(-\frac{\sqrt{3}}{6}\epsilon, -\frac{\epsilon}{2} \right) \quad .$$

Because each of the vertices are on the surface of the sphere, each must satisfy the equation $x^2 + y^2 + z^2 = r^2$. In each case, $z = \sqrt{r^2 - \frac{1}{3}\epsilon^2}$. Thus, each point on the triangle lies on the plane $z = \sqrt{r^2 - \frac{1}{3}\epsilon^2}$ and, in particular, M is on this plane. Since the radius of the sphere is r, the distance between the point on the sphere which is hit by $\overrightarrow{\vartheta M}$ and M is

$$r - \sqrt{r^2 - \frac{1}{3}\epsilon^2} \quad .$$

□

The triangles that are used in the Sphere Projection method are nearly equilateral and in no triangle is the length of a side greater than the chosen ϵ value. Thus, the error bound for the deviation of the sphere projection method is at most the error bound of the theorem using equilateral triangles with sides of length epsilon. Figure (3.2) gives examples of the triangulation of the sphere using ϵ values of 0.75, 0.45, 0.15, and 0.03, respectively. Assuming that a unit sphere was used in the calculations, the deviation associated with each of these values is 0.0425729, 0.0151142, 0.006689, and 0.0000667. In the applications to follow, the surfaces are captured through projection of the sphere triangulated by triangles with sides of length at most $\epsilon = 0.03$. To refine the resolution, a sphere triangulation of $\epsilon = 0.02$ was also used, providing a deviation value of 0.0000167. Although the ability for the VRML browsers to work with a file of such size is often limited by the amount of RAM of the computer, this larger triangulation makes it possible to view with better resolution a localized area of the surface.

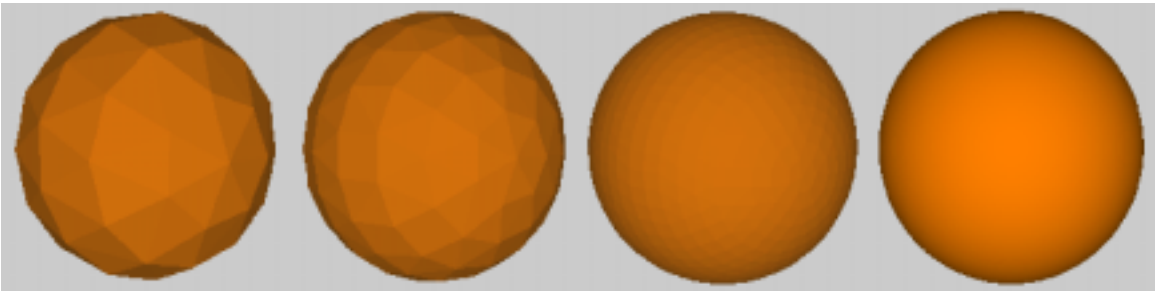

Figure 3.2: Spheres triangulated from 86, 188, 1322, and 31,860 points, respectively.

3.3 Projection of the Sphere onto the Desired Surface

Now that the unit sphere has been successfully triangulated, the next step is the projection of the sphere onto the surfaces that is to be represented. Given a function $F(\mathbf{X}) = \mathbf{0}$, for which the resulting surface is closed and convex, the goal is to project the triangulated unit sphere onto the surface defined by F so that a three-dimensional representation of the surface

is obtained. This method requires that a center point be chosen and denoted by C. Clearly, this point should not be on the surface.

Using the list of points that was collected during the sphere triangulation process completed in the previous section, create an array S in which $S(k)$ represents the vector from the origin to the kth point in the list. $S(k)$ is first normalized. Create a new point $X = C + S(k) * T$ where T will be varied by small increments until a point sufficiently close to the desired surface is found. The functional value of X is then evaluated at each T until consecutive T's, call them $\bar{T}$ and $\hat{T}$, produce a sign change. When this occurs, the value of t that projects $S(k)$ to the surface falls in the interval $(\bar{T}, \hat{T})$ and is found using a bisection method. The point $X = C + S(k) * t$ is the point on the desired surface that corresponds to the point on the unit sphere that is associated with $S(k)$. The coordinates of this point are then recorded. This process is repeated for all points in the list derived from the triangulation.

In this description of the process, F was assumed to define a nice closed and convex surface. In reality, F may actually define a family of surfaces. This is indeed the case of the Laplacian surfaces, where the function is viewed as a collection of concentric shells. When this is the situation at hand, it may be necessary to count the shells so that the desired shell is the one that is represented and so that leaps from one surface to another are avoided.

3.4 Modeling the Zero Laplacian Surfaces of H_2O

The Sphere Projection Method was applied to the Zero Laplacian surfaces of water. The results were encouraging. Figure (3.3) shows the middle shell of the Zero Laplacian facing the plane containing the oxygen and hydrogen molecules.

Since this surface strongly resembled the expected shape, an attempt was made to

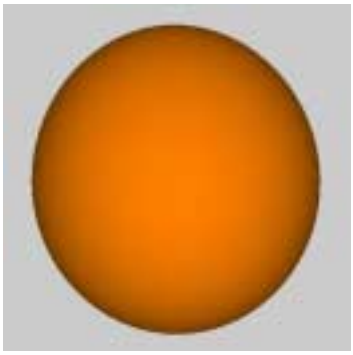

Figure 3.3: Middle zero Laplacian shell of water.

capture the outer Zero Laplacian surface. Because this surface is not convex, as can be seen in Figure (3.1), the ability to model this surface was in question. The results, however, were exciting and unexpected. Figure (3.4) shows the outer Zero Laplacian shell of water. Surprisingly, the only areas on the outer Zero Laplacian shell where the Sphere Projection method had any difficulty in representing the surface were in the small areas that display "stretch marks". These areas are the result of the projection of the sphere onto a surface that is not convex. Figure (3.5) shows that even though we are starting with triangles whose sides are small on the sphere, the triangle on the surface obtained from the projection may have much larger sides. How bad can the error actually be? Suppose the surface to be modeled is a sphere of radius one and that the triangulation is composed of nonequilateral triangles. Let ΔXYZ be such a triangle. Let XY be the largest side of ΔXYZ and denote the length of XY by γ. Note that XY forms a chord of the great circle through X and Y. Let P be any point on XY. Let the deviation now be defined as the distance from the point P to the point on the sphere pierced by the radial extention that passes through P. The midpoint of the chord is then the point of greatest deviation to the circle's boundary. Thus, a small amount of algebra reveals that the deviation is at most

$$r - \sqrt{r^2 - \frac{1}{4}\gamma^2} \quad .$$

The actual deviation for any point on the triangle can possibly be worse than this value.

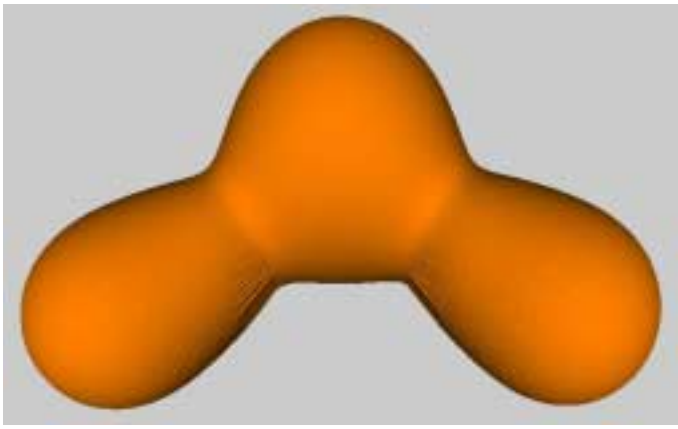

Figure 3.4: Outer zero Laplacian shell of water.

To further understand the importance of the problem of using this method on a surface that is not convex, one might consider an equilateral triangle whose sides are of length $\epsilon = 0.3$. The deviation value, as defined for Theorem 1, for such a triangle is 0.006689. This triangle has an area of approximately 0.03897 square units. A triangle, such as the one in the previous paragraph, that has the same area but with a side of length $5 * \epsilon = 1.5$ will have a deviation of 0.133975. This is a substantial increase from the deviation value of the equilateral triangle. Thus the accuracy of the representation is much more in doubt. It can be concluded then that the Sphere Projection method works extremely well if the desired surface is spherical or nearly so. Any surface containing holes or overlaps, or that is less convex than the Zero Laplacian surface of water, would fail to be accurately modeled using the Sphere Projection method.

Figure 3.5: Example of a problem with the Sphere Projection method on the water molecule.

Chapter 4

Using the Chicken Wire Method to Model Surfaces

Although the Sphere Projection method works well on closed convex surfaces, it fails to give a good representation of surfaces that are not closed or not convex. Many of the Laplacian surfaces of interest fall in this category. To capture these surfaces, the *Chicken Wire* method was created. The algorithms implemented in this method use the idea of molding chicken wire to a surface to capture the shape of the surface.

4.1 The Triangulation of the Hexagon

Given a point P, the first step in the Chicken Wire method is to construct an algorithm that will create a triangulation for an arbitrary number of hexagonal rings centered around P. Figure (4.1) shows an example of the hexagonal ring pattern that is used to begin the triangulation.

The triangulation pattern is created by extending the idea that one hexagon is formed from the composition of 6 equilateral triangles. These six triangles form the first elements of the triangulation. To triangulate the next ring, the line segments that bisect the first hexagon

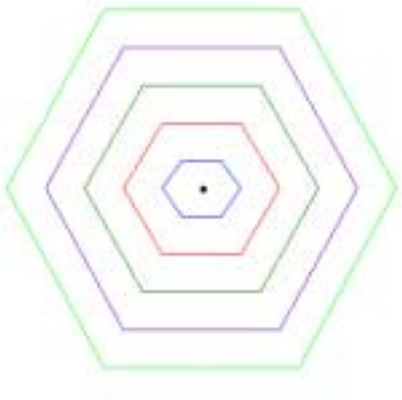

Figure 4.1: Hexagonal ring pattern.

Figure 4.2: Triangulating the hexagonal rings.

and help to form the six triangles are extended to the corners of the next hexagon as shown in Figure (4.2). The remaining line segments that form the edges of the inner hexagon are also extended until they intersect the second hexagonal ring. This fully triangulates the second hexagon. This pattern is extended to each successive hexagonal ring. The general algorithm is now given.

> Suppose N hexagonal rings are computed. Let the origination point be point 0. Label the points on the hexagonal rings by extending the pattern shown in Figure (4.3). The first six triangles are formed by the following triples:
>
> {0, 1, 2}; {0, 2, 3}; {0, 3, 4}; {0, 4, 5}; {0, 5, 6}; {0, 6, 1}.

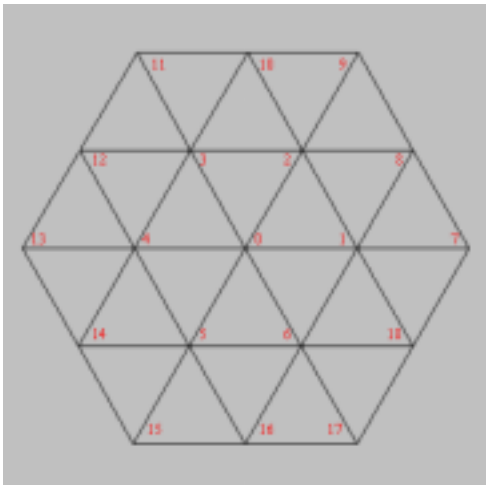

Figure 4.3: Labeling the triangulation vertices.

This triangulates the innermost hexagon. Now to triangulate the $N-1$ remaining hexagonal rings. Define

$$v(K,I) = 3(K-1)(K-2) + I \quad .$$

For K = 2, N-1

Let I = 1.
Form the following triangles:

{v(K,I), v(K+1, 6K), v(K+1,I)};
{v(K,I), v(K+1, I), v(K+1,I+1)};
{v(K,I), v(K+1, I+1), v(K,I+1)}.
Let I = I+1

For I = 2 to K-1

{v(K,I), v(K+1, I), v(K+1,I+1)};
{v(K,I), v(K+1, I+1), v(K,I+1)}.
Let I = I+1

For I = K

{v(K,I), v(K+1, I), v(K+1,I+1)};
{v(K,I), v(K+1, I+1), v(K+1,I+2)};
{v(K,I), v(K+1, I+2), v(K,I+1)}.
Let I = I+1

For I = K+1 to 2K-3

{v(K,I), v(K+1,I+1), v(K+1,I+2)};
{v(K,I), v(K+1, I+2), v(K,I+1)}.
Let I = I+1

For I = 2K-1

{v(K,I), v(K+1, I+1), v(K+1,I+2)};
{v(K,I), v(K+1, I+2), v(K+1,I+3)};
{v(K,I), v(K+1, I+3), v(K,I+1)}.
Let I = I+1

For I = 3K-2

{v(K,I), v(K+1, I+2), v(K+1,I+3)};
{v(K,I), v(K+1, I+3), v(K+1,I+4)};
{v(K,I), v(K+1, I+4), v(K,I+1)}.
Let I = I+1

For I = 3K-1 to 4k-4

{v(K,I), v(K+1, I+3), v(K+1,I+4)};
{v(K,I), v(K+1, I+4), v(K,I+1)}.
Let I = I+1

For I = 4K-3

{v(K,I), v(K+1,I+3), v(K+1, I+4)};
{v(K,I), v(K+1, I+4), v(K+1,I+5)};
{v(K,I), v(K+1, I+5), v(K,I+1)}.
Let I = I+1

For I = 4K-2 to 5K-5

{v(K,I), v(K+1, I+4), v(K+1,I+5)};
{v(K,I), v(K+1, I+5), v(K,I+1)}.
Let I = I+1

For I = 5K-4

{v(K,I), v(K+1,I+4), v(K+1, I+5)};
{v(K,I), v(K+1, I+5), v(K+1,I+6)};
{v(K,I), v(K+1, I+6), v(K,I+1)}.
Let I = I+1

For I = 5K-3 to 6K-7

{v(K,I), v(K+1, I+5), v(K+1,I+6)};
{v(K,I), v(K+1, I+6), v(K,I+1)}.
Let I = I+1

For I = 6k-6

{v(K,I), v(K+1, I+5), v(K+1,I+6)};
{v(K,I), v(K+1, I+6), v(K,1)}.
If (K=2) also form the triangle {v(K,I), v(K+1, I+4), v(K+1,I+5)}.

End of Algorithm.

Figure(4.4) shows an example of a piece of chicken wire that has been triangulated. It is now necessary to calculate the position of the vertices on the surface of interest.

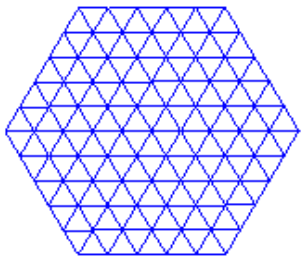

Figure 4.4: Chicken wire

4.2 Finding the starting vectors for the hexagonal system

The next step of the Chicken Wire method defines how the triangulation pattern described in the previous section becomes part of the surface. This is accomplished by finding initial vectors that will create the hexagonal system that will be manipulated in such a way so that the vertices of the triangulation are points on the desired surface. By choosing ϵ, the length of the sides of the triangles, to be sufficiently small, this method will allow the representation of almost any type of surface requiring only a point P that is located on the surface.

The first step in finding these initial vectors requires the calculation of the unit normal vector. Call the original basis D_1. Given a function F_1 and a point $[P(x, y, z)]_{D_1}$ on the surface defined by the equation $F_1 = 0$, the normal vector, $[\nabla F_1]_{D_1}$, to the surface at $[P]_{D_1}$ is calculated using a central difference method [9]. For a 3-dimensional surface, the ith component of the normal vector is given by

$$[\nabla F_1(i)]_{D_1} = \frac{F_1(\vec{x} + \epsilon * e_i) - F_1(\vec{x} - \epsilon * e_i)}{2 * \epsilon}$$

where e_i is the unit vector with all entries 0 except for the ith entry which is a 1. $[\nabla F_1]_{D_1}$ is then normalized so that it has unit length. Call this vector $[\vec{n}]_{D_1}$.

An orthonormal basis, D_2 is then created so that $[P]_{D_1}$ is the origin in D_2 and $[\vec{n}]_{D_2}$ is now pointing along the positive z-axis. Next the program determines a vector $[\vec{A}]_{D_2}$ of magnitude ϵ that is perpendicular to $[\vec{n}]_{D_2}$. Choose $[\vec{A}]_{D_2}$ to be the vector of length ϵ that points along the positive x-axis. Working in spherical coordinates, $\theta = 0$ and $\phi = \frac{\pi}{2}$. To create the hexagonal system, $[\vec{B}]_{D_2}$ needs to be chosen at a 120° angle to $[\vec{A}]_{D_2}$ and perpendicular to $[\vec{n}]_{D_2}$. Let $\theta_B = \frac{2\pi}{3}$. Then

$$[\vec{B}]_{D_2} = (\epsilon * \sin\phi * \cos\theta_B, \epsilon * \sin\phi * \sin\theta_B, \epsilon * \cos\phi) \quad .$$

$[\vec{A}]_{D_2}$ and $[\vec{B}]_{D_2}$ are the vectors that will develop the hexagonal system.

4.3 Creating the First and Second Hexagonal Rings

The point P provided to the algorithm initially is considered to be the first hexagonal ring. The second hexagonal ring will be composed of six points found from calculations using $[\vec{A}]_{D_2}$ and $[\vec{B}]_{D_2}$. If the surface was planar, the points would be represented by the direction vectors, $[\vec{A}]_{D_2}$, $[\vec{A}+\vec{B}]_{D_2}$, $[\vec{B}]_{D_2}$, $[-\vec{A}]_{D_2}$, $[-\vec{A}-\vec{B}]_{D_2}$, and $[-\vec{B}]_{D_2}$. Since the goal is to place the hexagon onto a nonplanar surface, these points must be altered so that each is actually on the surface . The steps that are necessary to ensure this fact for any of the six points of the second hexagonal ring are now given in detail.

The process begins with finding the point P_A on the surface that corresponds with $[\vec{A}]_{D_2}$. From the definition of spherical coordinates, θ is the angle formed from the vector

with the x-axis and is held constant throughout the search for the P_A. ϕ, on the other hand, will be allowed to take on incremental values between $[0, 2\pi)$. A new point $[P_{temp}]_{D_2}$ is chosen so that

$$[P_{temp}]_{D_2} = (\epsilon * \sin\phi * \cos\theta, \epsilon * \sin\phi * \sin\theta, \epsilon * \cos\phi) \quad .$$

$[P_{temp}]_{D_2}$ is then changed back into the original basis, D_1 and the functional value for the point is calculated. The values of $F([P_{temp}]_{D_1})$ are monitored for a sign change. When this occurs, the interval is noted and the actual value of ϕ is found using a bisection method. Call this value $\bar{\phi}$. Then $[P_A]_{D_1}$ is a point on the desired surface which corresponds to $[\vec{v}]_{D_2}$ with the value

$$[P_A]_{D_2} = (\epsilon * \sin\bar{\phi} * \cos\theta, \epsilon * \sin\bar{\phi} * \sin\theta, \epsilon * \cos\bar{\phi}) \quad .$$

The above steps are repeated for each of the six direction vectors. The results are a set of six points, $\{P_A, P_{A+B}, P_B, P_{\_}, P_{-A-B}, P_{-B}\}$, which lie on the desired surface and form the second hexagonal ring.

4.4 How do you find a general point on the surface?

The algorithm uses the points on the kth ring to act as an origin for the calculation of the points on the $(k+1)$st ring. The positions of the points are found by the algorithm according to the numbering shown in Figure (4.3). Since the origin is constantly being changed from one point on the previous ring to another, the origin will always need to be specified and will be denoted as ϑ. In addition, a vector v is provided to determine the direction the corresponding point on the surface should lie. The process then is as follows:

> Given ϑ, a new orthonormal basis D_2 is created so that ϑ is the origin and the normal to the surface through ϑ points along the x-axis. The vector v is placed

at the origin. The values of θ, ϕ, and $\bar{\phi}$ are found as described in the previous section. From these value, $[P_{new}]_{D_2}$ is defined by

$$[P_{new}]_{D_2} = (\epsilon * \sin\bar{\phi} * \cos\theta, \epsilon * \sin\bar{\phi} * \sin\theta, \epsilon * \cos\bar{\phi}) \quad .$$

$[P_{new}]_{D_1}$ is the point on the surface that corresponds to ϑ and v.

4.5 The Algorithm for Growing the Hexagonal Net

Now that the general method for finding a point on the surface which corresponds to a chosen origin and a direction vector has been described, the algorithm that describes how each hexagonal ring grows from the previous ring is now given. In this algorithm, $H_{i,j}$ represents the position of the jth point on the ith hexagonal ring. Also, $V_{i,j}$ represents the direction vector to the point $H_{i,j}$ from the point on the previous ring that was used in the calculations to create $H_{i,j}$. With the notation defined, the growth algorithm can now be given.

Let N be the number of hexagonal rings to be calculated.
Let $k = 3, N$.

Let $I = 1$.
Let $II = 1$

Let $\vartheta = H_{k-1,II}$.
Let $v = V_{k-1,II}$.
Find $H_{k,I}$ and $V_{k,I}$.
Let $I = I + 1$.

Let $II = 1, k-1$

If $II = k-1$, then define $III = k-1$. Else, let $III = II + 1$.
Let $\vartheta = H_{k-1,III}$.
Let $v = V_{k-1,II}$.
Find $H_{k,I}$ and $V_{k,I}$.
Let $I = I + 1$.

Let $II = k-1, 2k-3$

If $II = 2k-3$, then define $III = 2k-3$. Else, let $III = II+1$.
Let $\vartheta = H_{k-1,III}$.
Let $v = V_{k-1,II}$.
Find $H_{k,I}$ and $V_{k,I}$.
Let $I = I + 1$.

Let $II = 2k-3, 3k-5$

If $II = 3k-5$, then define $III = 3k-5$. Else, let $III = II+1$.
Let $\vartheta = H_{k-1,III}$.
Let $v = V_{k-1,II}$.
Find $H_{k,I}$ and $V_{k,I}$.
Let $I = I + 1$.

Let $II = 3k-5, 4k-7$

If $II = 4k-7$, then define $III = 4k-7$. Else, let $III = II+1$.
Let $\vartheta = H_{k-1,III}$.
Let $v = V_{k-1,II}$.
Find $H_{k,I}$ and $V_{k,I}$.
Let $I = I + 1$.

Let $II = 4k-7, 6(k-2)$

If $II \geq 5k-9$, then define $III = II$. Else, let $III = II+1$.
Let $\vartheta = H_{k-1,III}$.
Let $v = V_{k-1,II}$.
Find $H_{k,I}$ and $V_{k,I}$.
Let $I = I + 1$.

Final Element: Let $II = 6(k-2)$.

Let $\vartheta = H_{k-1,1}$.
Let $v = V_{k-1,6(k-2)}$.
Find $H_{k,6(k-1)}$ and $V_{k,6(k-1)}$.

End of Algorithm.

4.6 The Chicken Wire Method: How Accurate Is It?

The Chicken Wire method was developed to overcome the limitations of the Sphere Projection method. Before a claim can be made that the Chicken Wire method is indeed the better method, however, it is necessary to show that this method accurately accomplishes its given task. The next section will show specific examples of surface representations, obtained

from the application of the Chicken Wire Method, that could not have been modeled by the Sphere Projection method. The faithfulness of those representations will now be addressed. The functions that are of interest in this project are all locally convex. With this knowledge and if the definition of deviation that was used to prove Theorem 1 is applied, the following corollary addresses the accuracy of this method.

Corollary 1. *Assume that ΔABC is an equilateral triangle with sides of length λ obtained through the implementation of the Chicken Wire method. If P is any point on ΔABC, then the deviation from any point on ΔABC to the corresponding point on the surface is*

$$r - \sqrt{r^2 - \frac{1}{3}\lambda^2} \quad .$$

Proof. Let ΔABC be an equilateral triangle defined in the Chicken Wire method and choose a point P on ΔABC. Let $\bar{P}$ be the point on the sphere that corresponds to the P as defined in Theorem 1. Let κ denote the absolute value of the mean curvature of the surface at $\bar{P}$. Since our surface is locally convex and by the definition of curvature, there exists a sphere of radius $\frac{1}{\kappa}$ that locally approximates the surface. Thus ΔABC fits the criteria for Theorem 1. Consequently, if $r = \frac{1}{\kappa}$ and λ equals the length of the sides of ΔABC, the corollary follows. □

Some limitations of the Chicken Wire method need also be addressed. If the absolute value of the curvature of the surface that is to be represented by the method is small, then the triangles developed by the Chicken Wire method are nearly equilateral and the corollary predicts the accuracy of the model. If, on the other hand, the curvature is large, the triangles may not be equilateral. They will, however, always be isosceles. In this case, the third side will be less than 2α if the other two sides have length α. Thus, it is guaranteed that the worst case scenario is that the deviation value of a point on this triangle will be less than

$$r - \sqrt{r^2 - \frac{1}{3}(2\alpha)} \quad .$$

This is not the case in any of the applications presented here, however. To handle this situation, the surface is broken into sections, each to be individually modeled and then the representations combined to form a complete model of the surface. This allows for ϵ to be varied depending on the curvature of the section of the surface. If the curvature value is great, then the value for ϵ used in the Chicken Wire method is chosen to be smaller than if the curvature value had been less. As a result, the accuracy of the model can be controlled regardless of the curvature values of points on the surface.

4.7 Applications

With the help of the Chicken Wire method, three-dimensional representations of surfaces that are not spherical and/or convex, but that have holes and strange curves, may be obtained. Such models could never be captured by the Sphere Projection method. Figure (4.5) is a representation of

$$\nabla^2\rho(r) = -19$$

isosurface of the molecule $NaLi_2Si_2OF_9$. This surface appears to be convex but it also has three holes. Figure (4.6) shows slices of this surface through the SiOSi plane and a plane perpendicular to the SiOSi plane, respectively. This surface is actually composed of two layers, something a projection method would not have discovered. The Chicken Wire method was able to capture an accurate representation of the surface, revealing the holes, the layers, and the change in the distance between the two layers as can be seen in Figure (4.6).

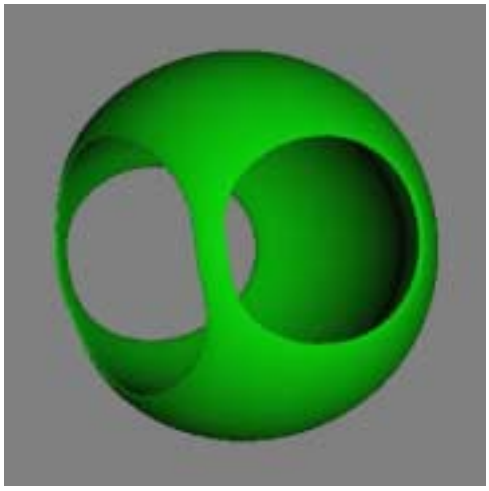

Figure 4.5: 3D representation $-\nabla^2\rho(\mathbf{r}) = 19$ of $NaLi_2Si_2OF_9$

Figure 4.6: 3D representation $-\nabla^2\rho(\mathbf{r}) = 19$ sliced through the SiOSi plane and a plane perpendicular to the SiOSi plane of $NaLi_2Si_2OF_9$

Chapter 5

Curvature

The curvature value of a given point on a surface plays an important role in the research presented in this dissertation. Understanding curvature allows for a significant improvement in the accuracy of the Chicken Wire method. In addition, the curvature of a mineralogical surface may also be an indicator of electronic behaviour. With this in mind, an algorithm was developed to calculate the curvature value of a point on a surface.

"Mean curvature" is defined to be the average of the principal curvatures, i.e. half the sum of the minimum curvature and maximum curvature values at a given point. Given a point S on a surface, these values are calculated with respect to the normal to the surface through this point. If this orientation is held and the two-dimensional Hessian, H, is calculated with respect to this orientation, the eigenvalues of the Hessian are the minimum and maximum curvature values. Because H is symmetric, the trace is the sum of the eigenvalues which is the sum of the principle curvatures of the surface at S. Thus to calculate the curvature at any point S on the surface, it is necessary to create an orthogonal basis with the normal through S to the surface as the kth vector. The Hessian is then calculated and the curvature value is obtained by taking half the trace. The following sections describes algorithms for these processes.

5.1 Computation of Orthogonal Basis

The first step in the calculations of the curvature at a given point P(x,y,z) on the surface obtained from the evaluation of a function $F_1(x, y, z) = 0$, is to calculate the normal vector, ∇F_1, to the surface at P using a central difference method [9]. For a 3-dimensional surface, the ith component of the normal vector is given by

$$\nabla F_1(i) = \frac{F_1(\vec{x} + \epsilon * e_i) - F_1(\vec{x} - \epsilon * e_i)}{2 * \epsilon}$$

where e_i is the unit vector with all entries 0 except for the ith entry which is a 1. ∇F_1 is then normalized so that it has unit length. Call the new unit vector $[\mathbf{k}]_{D_1}$ where D_1 represents the original basis of our surface calculations.

To calculate the curvature of the surface at the point P, it is necessary to construct an orthonormal basis D_2 composed of $[\mathbf{k}]_{D_1}$ and two other unit vectors, forming a mutually orthogonal basis. First, a perpendicular vector to $[\mathbf{k}]_{D_1}$ is constructed. This vector is chosen according to the method given by Boisen and Gibbs [8]. The vector is then normalized and will be denoted by $[\vec{i}]_{D_1}$,

Since the vector $[\vec{i}]_{D_1} \times [\vec{k}]_{D_1}$ is orthogonal to both $[\vec{i}]_{D_1}$ and $[\vec{k}]_{D_1}$, let

$$[\vec{j}]_{D_1} = \frac{[\vec{i}]_{D_1} \times [\vec{k}]_{D_1}}{\left\| [\vec{i}]_{D_1} \times [\vec{k}]_{D_1} \right\|} \quad .$$

Then i, j, k form the new basis, D_2. The matrix T^{-1} is created from the vectors i, j, k by

$$T^{-1} = \left[[\vec{i}]_{D_1} \;\middle|\; [\vec{j}]_{D_1} \;\middle|\; [\vec{k}]_{D_1} \right] \quad .$$

By inverting T^{-1}, the matrix T is found so that $T[\mathbf{r}]_{D_1} = [\mathbf{r}]_{D_2}$. This now allows for the curvature calculations.

5.2 Computation of the Hessian

After the required orthonormal basis has been calculated, the next step is to calculate the Hessian. The original point $P(x, y, z)$ is written with respect to the new D_2 basis using the matrices T and T^{-1}. Ignoring the new z-component of the point, create a two-dimensional vector from the first two coordinates of the point, call it $\vec{x}$. A second function must be now be defined. This two-dimensional function, $F_2(x, y) = z$, calculates a z-value for each ordered pair so that the point (x, y, z) is on the surface defined by $F_1 = 0$. The function F_2 will be used in the function calculations of the Hessian. Because the trace is required, only the diagonal elements of the Hessian are needed. Since the functional values that must be calculated are not analytically available, however, a finite difference approximation is utilized in the process [9]. The diagonal values of the Hessian, H, are defined as

$$H_{ii} = \frac{F_2(\vec{x} + 2\epsilon * e_i) - 2F_2(\vec{x} + \epsilon * e_i) + F_2(\vec{x})}{\epsilon^2} \quad .$$

The trace of the Hessian then is simply $H_{11} + H_{22}$ and the mean curvature, κ, is half the trace.

5.3 Applications to the Study of Mineralogy

Unfortunately, not enough information has been gathered to fully understand the role in the study of molecular models of crystals of the curvature of the Zero Laplacian isosurfaces. Because the shells of the Laplacian have been shown to hold so much information about the crystal, it would seem that the curvature of the Zero Laplacian might be able to share some of the secrets that the Laplacian of the electron density function holds.

Figures (5.1) and (5.2) shows a representation of the$-\nabla^2\rho(\mathbf{r}) = 0e/\mathring{A}^5$ and the

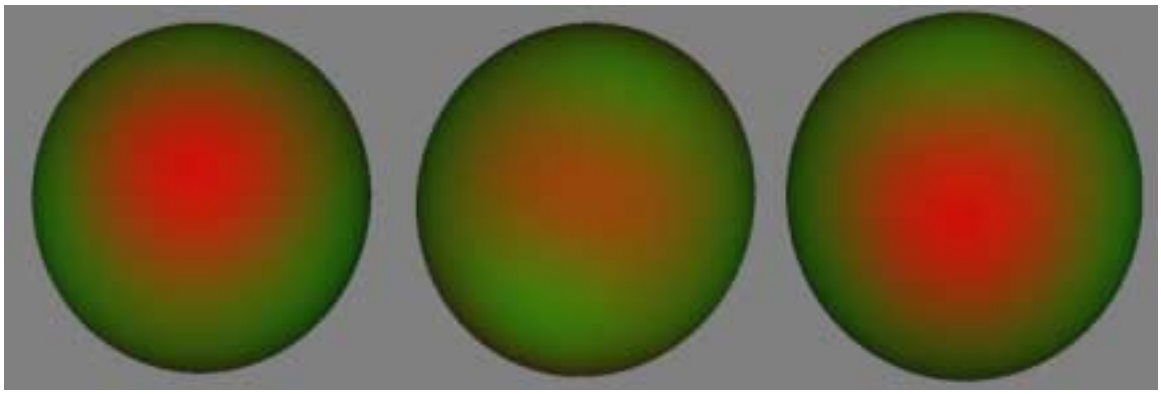

Figure 5.1: 3-Dim representations of the Zero Laplacian isosurface of $NaLi_2Si_2OF_9$

$-\nabla^2\rho(\mathbf{r}) = 19e/\mathring{A}^5$ shells of the Laplacian, respectively. Coloration is applied to the zero shell according to the value of the curvature of the Laplacian of the electron density function. The color scheme ranges from green to red with green representing the areas of lowest curvature and red representing the areas of highest curvature. Figure (5.3) shows the combination of the representations of these two shells. Note that for each area of highest curvature on the zero shell, a hole is in existence on the $-\nabla^2\rho(\mathbf{r}) = 19e/\mathring{A}^5$ isosurface. This would indicate some relation between the curvature and the formation of the shape of subsequent shells.

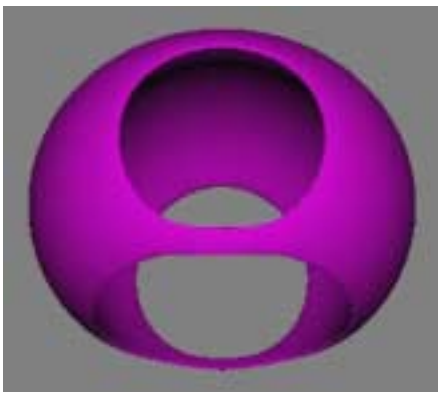

Figure 5.2: 3-Dim representations of the -19 Laplacian isosurface of $NaLi_2Si_2OF_9$.

Examination of the disiloxane molecule reveals a similar pattern. Figures (5.4) and (5.5) shows a representation of the$-\nabla^2\rho(\mathbf{r}) = 0e/\mathring{A}^5$ and the $-\nabla^2\rho(\mathbf{r}) = 15e/\mathring{A}^5$ shells of the Laplacian of the electron density function of $H_6Si_2O_7$, respectively. Coloration is again

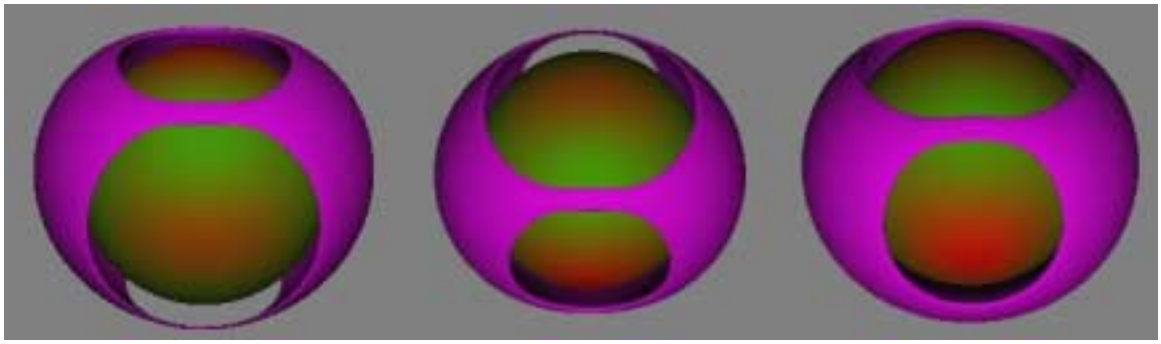

Figure 5.3: 3-Dim representations of the -19 Laplacian isosurface and the Zero Laplacian isosurface of $NaLi_2Si_2OF_9$ graphed together.

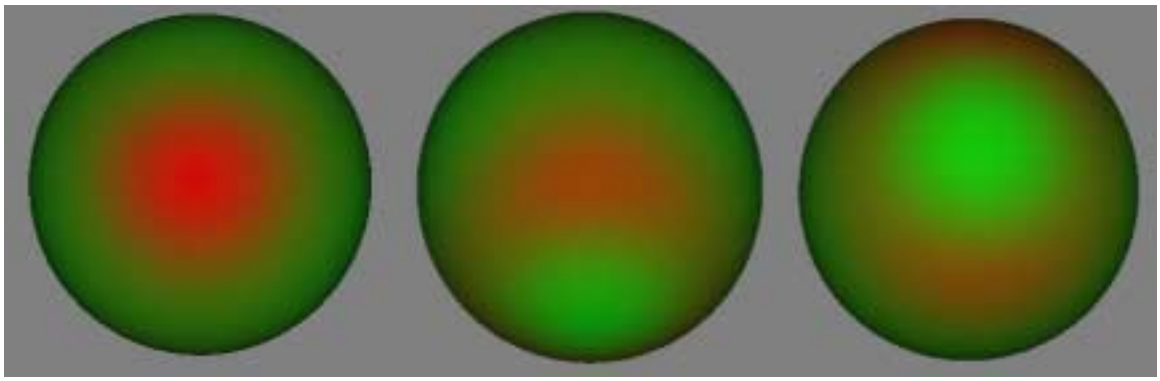

Figure 5.4: 3-Dim representations of the Zero Laplacian isosurface of $H_6Si_2O_7$

applied to the zero shell according to the value of the curvature of the Laplacian of the electron density function. As with the previous molecule, the color scheme ranges from green to red with green representing the areas of lowest curvature and red representing the areas of highest curvature. Figure (5.6) shows the combination of the representations of these two shells. The results are exact to those of the molecule $NaLi_2Si_2OF_9$. For each area of highest curvature on the zero shell, a hole is in existence on the $-\nabla^2\rho(\mathbf{r}) = 15e/\mathring{A}^5$ isosurface. Consequently, since a similar observation has occurred for two different molecules, a relationship between the curvature of the Zero Laplacian isosurface and the subsequent shells seems to exist.

As of this time, insufficient data has been collected to conclude any connections

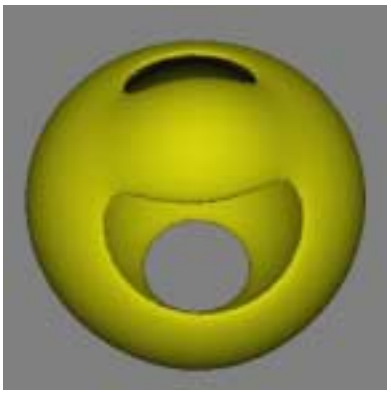

Figure 5.5: 3-Dim representations of the -15 Laplacian isosurface of $H_6Si_2O_7$.

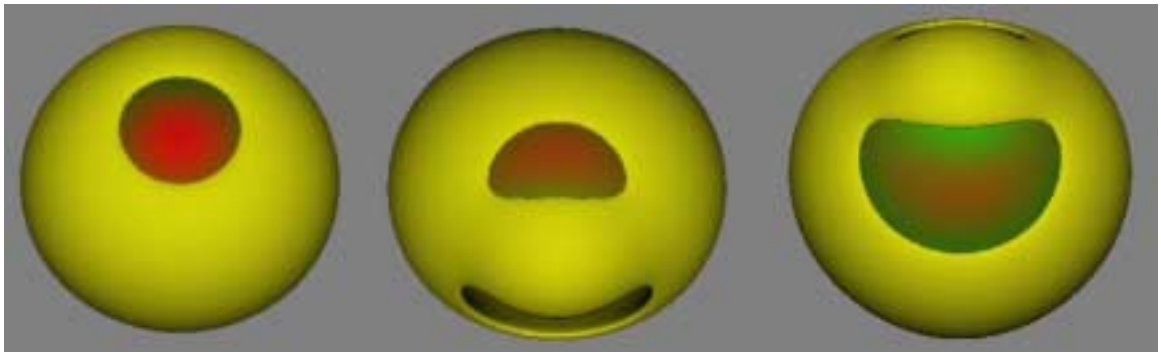

Figure 5.6: 3-Dim representations of the -15 Laplacian isosurface and the Zero Laplacian isosurface of $H_6Si_2O_7$ graphed together.

between the curvature of the Zero Laplacian surfaces and the shape of other isosurfaces. Based on the information provide here about the molecules $H_6Si_2O_7$ and $NaLi_2Si_2OF_9$, a relationship is indicated, however. Consequently, further studies need to be completed and the results analyzed. If such an association is deduced, the curvature of the Zero Laplacian surfaces of a molecule may then be used as a tool to predict the behavior of other isosurfaces of the Laplacian of the electron density function.

Chapter 6

Applications to the Laplacian

Theoretically, all of the information needed to understand bonding in minerals is present in the electron density distribution, $\rho(r)$. However it is very difficult to appreciate the subtle but important variations in $\rho(r)$ by viewing it directly. Direct examination of $\rho(\mathbf{r})$ generally only reveals a peak at the positions of the nuclei and thus little knowledge is gained from visual inspection of $\rho(r)$[17]. The Laplacian, $\nabla^2\rho(\mathbf{r})$, is capable of revealing the more subtle features of $\rho(r)$. Loosely speaking, the Laplacian measures the "lumpiness" of ρ.

The fact that electrons are arranged in a shell formation within a molecule is an accepted one. Unfortunately, these shells cannot be seen by direct examination of $\rho(r)$. These shells are clearly defined, on the other hand, in the Laplacian distribution. Concentric shells that alternate as areas of local concentration and depletion with the outermost shell of locally concentrated electron density being referred to as the valence shell charge concentration, VSCC, of the atom are revealed through the examination of the Laplacian distribution [13]. The areas of local concentration and local depletion, defined by Bader [5] to be the regions where $\nabla^2\rho(\mathbf{r}) < \mathbf{0}$ and $\nabla^2\rho(\mathbf{r}) > \mathbf{0}$, respectively, are depicted along with the corresponding maxima and minima. Because $\nabla^2\rho(\mathbf{r}) < \mathbf{0}$ corresponds to an area of local concentration, it is common to discuss the negative Laplacian, $-\nabla^2\rho(\mathbf{r})$. Thus, studies are

normally conducted around the direct correspondence that $-\nabla^2\rho(\mathbf{r}) > \mathbf{0}$ designates a region of local concentration.

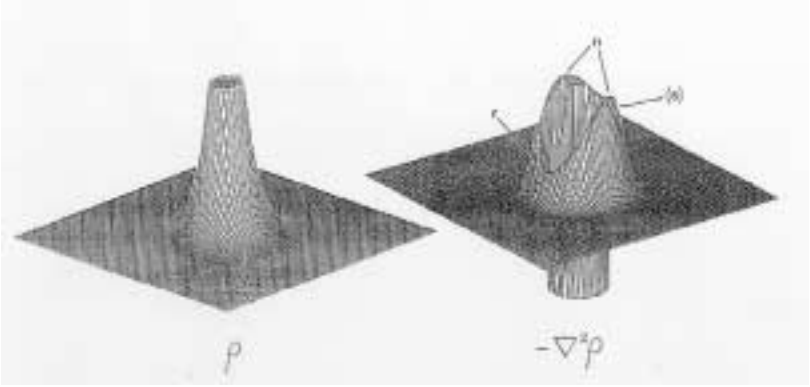

Figure 6.1: Relief maps of the total charge density and the Laplacian for the water molecule in the plane $\perp$ to HOH plane. Images taken from MacDougall [17].

For comparison, Figures (6.1) and (6.2) are relief maps taken from MacDougall [17] of $\rho(\mathbf{r})$ and $-\nabla^2\rho(\mathbf{r})$ of the water molecule. Figure (6.1) shows the plane perpendicular to the HOH plane. The charge density, ρ, exhibits a single peak at the oxygen nucleus. The Laplacian, however, shows two shells of charge concentration. According to the VSCC, two maxima can be found in this plane. The points labeled **r** and **s** denote saddle points of the Laplacian. Figure (6.2) shows the HOH plane. The charge density exhibits a peak at each nucleus, as does the Laplacian, but the Laplacian also has a peak (labeled **b**) corresponding to a bonded maximum along each bond [17].

The Laplacian shows up in some unexpected places. In 1969, Bader and Preston [17] gave two expressions for kinetic energy density that each yield the total kinetic energy when integrated over all space. Locally, however, the two are very different and are defined as

$$K(r) = -\left(\frac{\hbar^2}{2m}\right)\sum_i \lambda_i\phi_i(r)\nabla^2\phi_i(r)$$

and

$$G(r) = \frac{\hbar^2}{2m}\sum_i \lambda_i\nabla\phi_i(r)\nabla\phi_i(r).$$

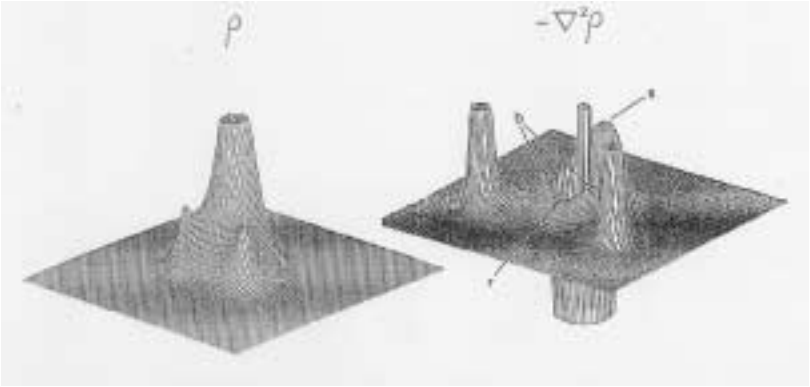

Figure 6.2: Relief maps of the total charge density and the Laplacian for the water molecule in the HOH plane. Images taken from MacDougall [17].

In both equations, ϕ_i represents the molecular orbitals, λ_i represents the occupation numbers of the orbitals, and m represents the non-relativistic mass of an electron. Locally $K(r)$ and $G(r)$ differ by amount proportional to the Laplacian of the electron density distribution function, i.e.

$$K(r) - G(r) = -\left(\frac{\hbar^2}{2m}\right)\nabla^2\rho(r).$$

The Laplacian was also shown to relate the kinetic energy density, $G(r)$, to the potential energy density, $v(r)$ [4]. In particular,

$$-\left(\frac{\hbar^2}{4m}\right)\nabla^2\rho(r) = 2G(r) + v(r).$$

Since the kinetic energy density term is always positive and the potential energy term is always negative, the sign of the Laplacian indicates which term is larger. This knowledge gives scientists a way to characterize interactions between atoms of a molecule in terms of the Laplacian of the electron density distribution function.

Knowledge of bonding interactions and reaction mechanisms within a molecular or crystal structure is crucial to the understanding of crystal chemistry, phase transformations, weathering, bacterial attack, and many other geochemical processes. With this in mind, theoretical electron density distributions of organic materials have been developed by chemical

physicists for the study of reaction mechanisms [5, 7, 6, 17]. In a study of these mechanisms for earth materials, theoretical electron density distributions are currently being calculated and evaluated for a variety of molecules and minerals at Virginia Tech by Boisen and Gibbs [12, 11, 13, 20]. The goal of these studies is to locate sites of local concentration and depletion of electron density that can be used to construct electronic reactivity maps. According to Hendrickson et al. [14], the maps serve to delineate sites in the substrates and reagents of potential electrophilic (locally electron rich) and nucleophilic (locally electron deficient) attack. Such sites can be found by evaluating the electron density distribution and determining the critical points of the negative Laplacian of the electron density distribution [5, 6]. Application of the Sphere Projection method and the Chicken Wire method to these studies will not only provide verification of known information but will also provide a means for a more in-depth visual study of the sites of interest leading to advancements in understanding of the underlying reaction processes.

6.1 Application to Water

Since water is a simple, well-studied molecule, it is a good molecule with which to test the development of the tools discussed in this work. Many studies have been completed on the water molecule and the electron density distribution has been fully examined. A calculation of the $-\nabla^2\rho(\mathbf{r})$ distribution for the water molecule reveals two lone pair and two bond pair local concentrations about the oxide anion. The two hydrogen atoms of the molecule lie on one side of the anion in a plane with the two bond pair and the two lone pair lie on the other in a perpendicular plane that bisects the HOH angle. Each lone pair (lp) is 0.40 Å from the anion and makes a lpOlp angle of 134.0°. In general, the more electron rich the lone pair, the greater they repel one another and the greater their distance apart and the wider the lpOlp angle. An unshared pair of electrons act as reactive sites that seek a positively charged or

electron deficient site in another molecule such as the hydrogen atom of an adjacent water molecule [14].

By utilizing the abilities of the Chicken Wire method and Sphere Projection method, a three-dimensional representation of the $-\nabla^2\rho(\mathbf{r})$ can now be obtained and a better perspective of the extent and overall shape of the lone pair local concentrations can be gained.

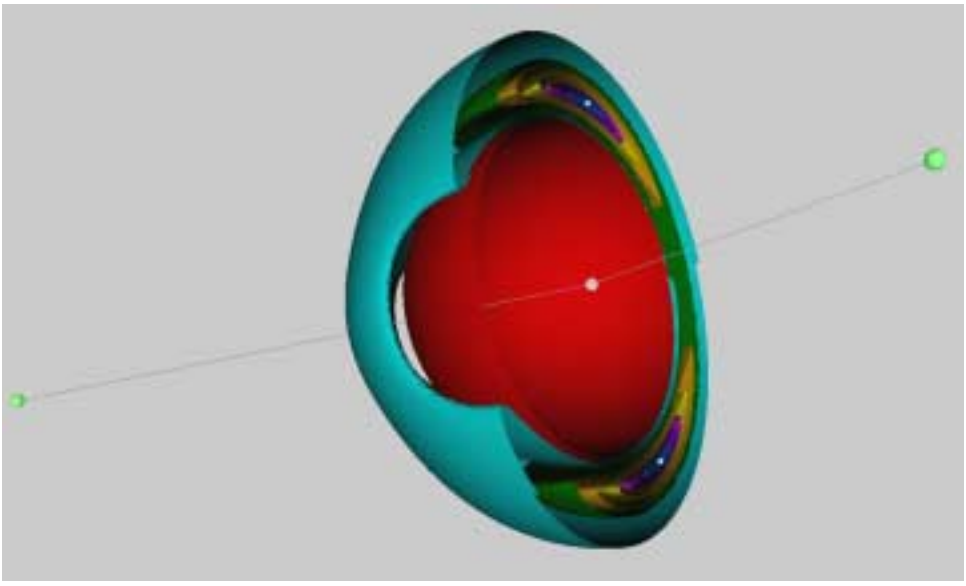

Figure 6.3: A section of the three-dimensional representation of the $-\nabla^2\rho(\mathbf{r})$ centered on the oxide anion of H_2O cut perpendicular to the HOH angle.

Figure (6.3) shows a section of the representation which is centered at the oxide anion and cut perpendicular to the HOH angle. According to the information given above, two lone pair local concentrations should be visible in this plane. The red envelope in the surface denotes the $-\nabla^2\rho(\mathbf{r}) = 0.0e/\mathring{A}^5$ isosurface; the teal denotes the $-\nabla^2\rho(\mathbf{r}) = 15e/\mathring{A}^5$ isosurface; the green denotes the $-\nabla^2\rho(\mathbf{r}) = 30e/\mathring{A}^5$ isosurface; the orange denotes the $-\nabla^2\rho(\mathbf{r}) = 35e/\mathring{A}^5$ isosurface; the yellow denotes the $-\nabla^2\rho(\mathbf{r}) = 40e/\mathring{A}^5$ isosurface; the pink denotes the $-\nabla^2\rho(\mathbf{r}) = 42e/\mathring{A}^5$ isosurface; the purple denotes the $-\nabla^2\rho(\mathbf{r}) = 43e/\mathring{A}^5$ isosurface; the blue denotes the $-\nabla^2\rho(\mathbf{r}) = 44e/\mathring{A}^5$ isosurface. The center white sphere represents the oxide anion; the green spheres represent the hydrogen atoms. Notice, in

particular, the concentric envelopes about the light blue spheres which are located above and below the oxide anion. These shells define the shape and position of the lone pair local concentrations of electron density for the oxide anion.

6.2 Application to $H_6Si_2O_7$

The importance of the disiloxane molecule $H_6Si_2O_7$, is well documented [12, 13, 10]. These studies have shown that the behavior of the silicon and oxygen atoms in $H_6Si_2O_7$ is very similar to the behavior of those same atoms in such crystals as quartz, cristobalite, and other silicates. Consequently the study of $H_6Si_2O_7$ has led to the discovery of interesting properties of the crystals in the silicate family. Figure (6.4) gives a ball and stick representation of the $H_6Si_2O_7$ molecule. The red, black, and green spheres represents the oxygen, silicon, and hydrogen atoms, respectively.

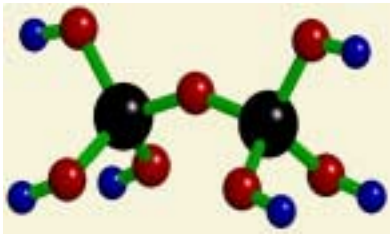

Figure 6.4: A ball and stick model of the molecule $H_6Si_2O_7$.

In a search for the local lone pair concentrations in the $H_6Si_2O_7$ molecule, a map was completed of the VSCCs for the oxide anions of the molecule [13]. The map was found to display one lone pair local concentration in the $-\nabla^2\rho(\mathbf{r})$ distribution at a distance of 0.35Å from the bridging oxide (O_{br}) anion, that is the oxygen that is bonded to the two silicon atoms. In contrast, each nonbridging oxide (O_{nbr}) anion is bonded to a silicon and a hydrogen cation and exhibits two lone pair concentrations. The lone pair together with the bridging oxide anion and the two silicon cations each lie in a common plane making

a lpO_{br}Si angle of 106.4° with both silicon cations. A deformation map calculated for the $H_6Si_2O_7$ molecule for a plane containing the SiOSi angle shows a single well-developed peak in the vicinity of the lone pair concentration displayed by the $-\nabla^2\rho(\mathbf{r})$ distribution.

Applying the Chicken Wire method and Sphere Projection method to the study of the $H_6Si_2O_7$ molecule not only gives verification of this information but also allows for a visual examination of the surfaces formed by the Laplacian function. The following color scheme will be maintained throughout the discussion of the bridging oxygen of the $H_6Si_2O_7$ molecule. The red envelopes in Figures (6.5) through (6.6) denotes the $-\nabla^2\rho(\mathbf{r}) = 0.0e/\mathring{A}^5$ isosurface; the blue denotes the $-\nabla^2\rho(\mathbf{r}) = 15e/\mathring{A}^5$ isosurface; the green denotes the $-\nabla^2\rho(\mathbf{r}) = 17e/\mathring{A}^5$ isosurface; the violet denotes the $-\nabla^2\rho(\mathbf{r}) = 22e/\mathring{A}^5$ isosurface; the yellow denotes the $-\nabla^2\rho(\mathbf{r}) = 24e/\mathring{A}^5$ isosurface. The white sphere contained in the innermost 0.0 isosurface represents the bridging oxide anion, while the dark grey spheres represents the silicon cations.

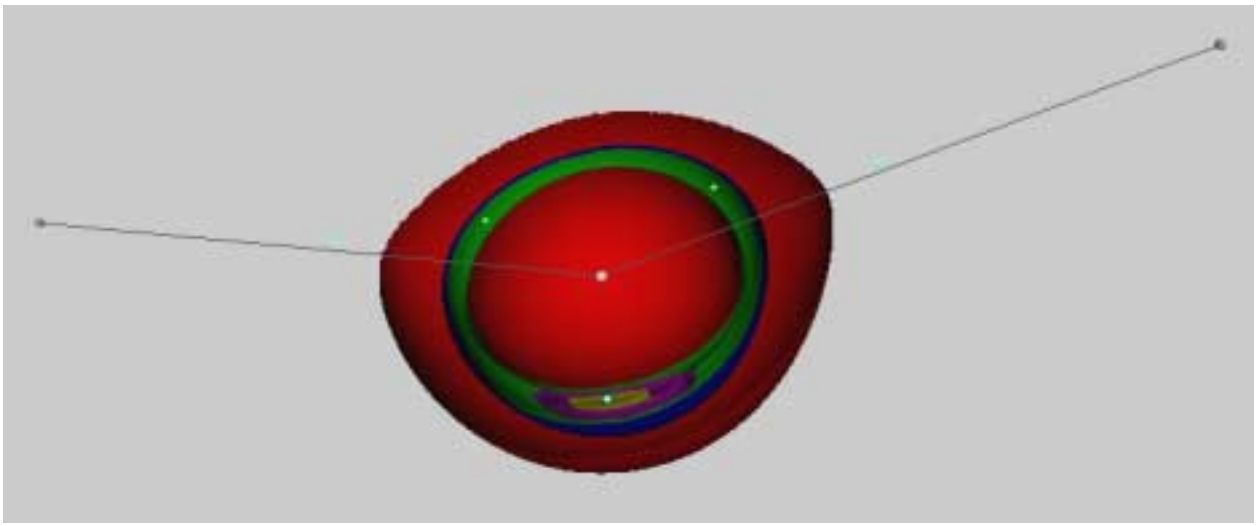

Figure 6.5: A section of the three-dimensional representation of the $-\nabla^2\rho(\mathbf{r})$ centered on the bridging oxide anion of $H_6Si_2O_7$ cut parallel to the SiOSi angle.

Figures (6.5) and (6.6) are representations of sections of the $-\nabla^2\rho(\mathbf{r})$ surface centered on the bridging oxide anion of $H_6Si_2O_7$. Figure (6.5) is a section cut parallel to the SiOSi angle while Figure (6.6) is a section cut perpendicular to the SiOSi angle. The concentric

envelopes about the yellow isosurface in Figure (6.5) defines the shape and position of the lone pair local concentration for the bridging oxide anion in the SiOSi plane. According to [10], examination of the resulting representations shows that lone pair concentration is highly localized in the plane directly above the anion as revealed by a mapping of the deformation $\nabla\rho(\mathbf{r}_c)$ distribution of the molecule. However, the disposition of the envelopes in Figure (6.6) indicates that the lone pair local concentration also extends to a considerable extent in a girdle in the plane perpendicular to the molecule. This implies that the lone pair local concentration associated with the bridging oxide anion is not only localized directly above the anion, but it is also highly elongated about the oxide anion in the plane perpendicular to the SiOSi angle. With this information, it can be concluded that when one of the acidic hydrogen atoms of a water molecule attacks the lone pair local concentration of a bridging oxide anion of $H_6Si_2O_7$, it will likely adopt a relatively wide range of positions along the girdle of the anion rather than adopting a single well-defined position.

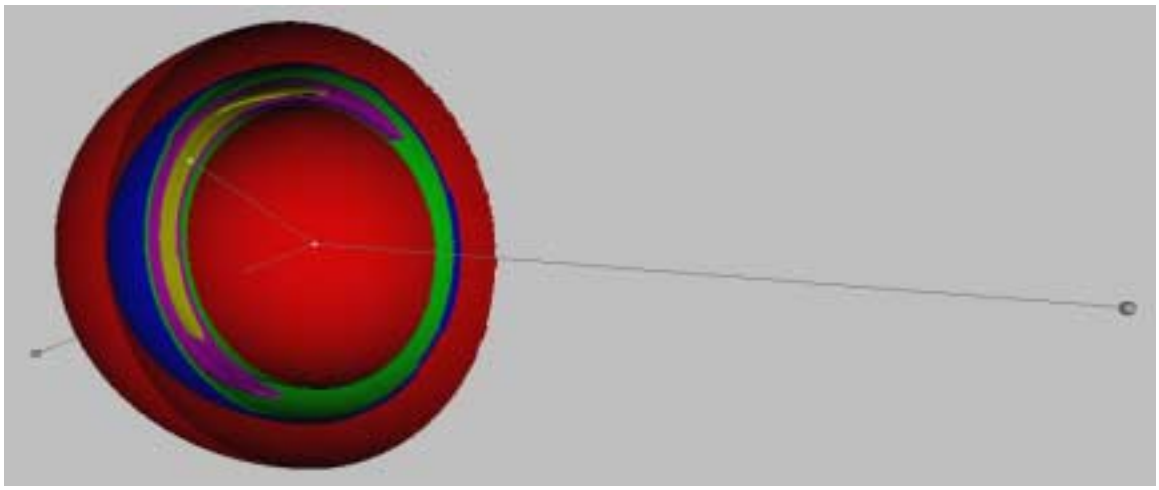

Figure 6.6: A section of the three-dimensional representation of the $-\nabla^2\rho(\mathbf{r})$ centered on the bridging oxide anion of $H_6Si_2O_7$ cut perpendicular to the SiOSi angle.

Figures (6.7) and (6.8) are representations of sections of the of the $-\nabla^2\rho(\mathbf{r})$ surface centered on the nonbridging oxide anion of $H_6Si_2O_7$. The following color scheme will be maintained throughout the discussion of the nonbridging oxygen of the $H_6Si_2O_7$ molecule.

The red envelopes in Figures (6.5) through (6.8) denotes the $-\nabla^2\rho(\mathbf{r}) = 0.0e/\mathring{A}^5$ isosurface; the teal denotes the $-\nabla^2\rho(\mathbf{r}) = 5e/\mathring{A}^5$ isosurface; the orange denotes the $-\nabla^2\rho(\mathbf{r}) = 10e/\mathring{A}^5$ isosurface; the blue denotes the $-\nabla^2\rho(\mathbf{r}) = 15e/\mathring{A}^5$ isosurface; the yellow denotes the $-\nabla^2\rho(\mathbf{r}) = 25e/\mathring{A}^5$ isosurface. The white sphere contained in the innermost 0.0 isosurface represents the nonbridging oxide anion, while the dark grey sphere represents the silicon cation and the green represents the hydrogen cation. Figure (6.7) is a section cut parallel to the SiOH plane while Figure (6.6) is a section cut perpendicular to the SiOH plane. In these representations, three envelopes define the positions of two bond pairs and one lone pair local concentrations. In Figure (6.7), note that the 15 isosurface is broken into three envelopes. Each envelope denotes occupation by either bond pair or lone pair local concentration. In this case, there are two bond pair local concentrations and one lone pair local concentration. The latter of the three is in the largest of the three envelopes. Figure (6.8) reveals that there is actually a second lone pair local concentration on each nonbridging oxide anion. The second lone pair local concentration is connected to the other lone pair by a girdle of local concentration of electron density very similar to the one presented in Figure (6.6). However, the girdle on the nonbridging oxide anion connects two lone pair maxima whereas the one on the bridging oxide anion involves only one lone pair maximum. The lone pair maxima, because of their larger sizes, are expected to be more susceptible to electrophilic attack than the bond pair maxima.

Although the information about the lone pairs was known, the Chicken Wire method and Sphere Projection method enhanced this knowledge by allowing visual examination of the $-\nabla^2\rho(\mathbf{r})$ surface. It was during this examination that the existence of the girdles of local concentration of electron density was discovered. These girdles, which had gone unnoticed in previous studies, were quite obvious to the naked eye in the three-dimensional representations obtained from application of the methods described in this dissertation to

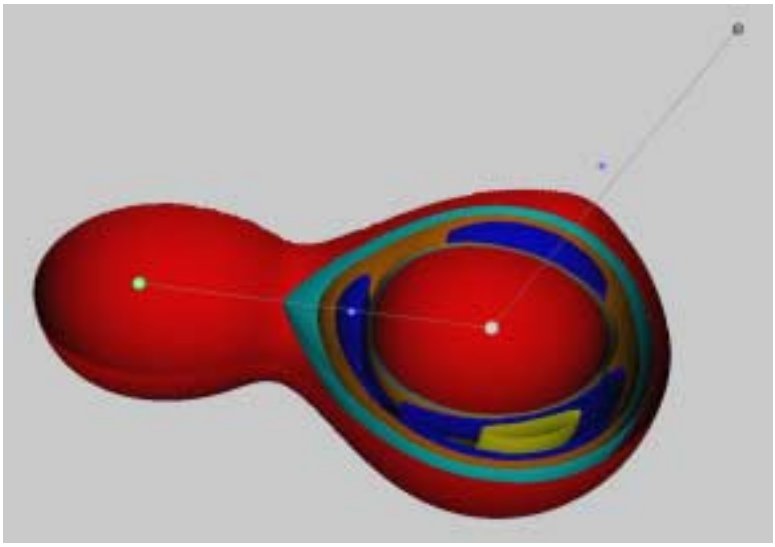

Figure 6.7: A section of the three-dimensional representation of the $-\nabla^2\rho(\mathbf{r})$ centered on the nonbridging oxide anion of $H_6Si_2O_7$ cut with the SiOH plane.

the $H_6Si_2O_7$ molecule. This extra piece of knowledge gives new insight into the identification of sites that are susceptible to nucleophilic and electrophilic attack.

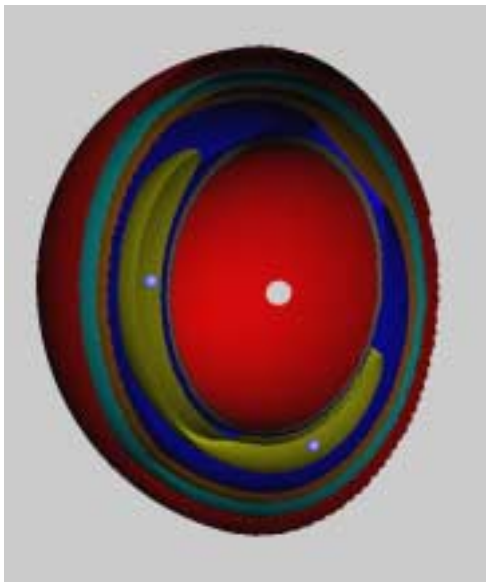

Figure 6.8: A section of the three-dimensional representation of the $-\nabla^2\rho(\mathbf{r})$ centered on the bridging oxide anion of $H_6Si_2O_7$ cut through a plane perpendicular to the SiOH plane.

6.3 Application to $NaLi_2Si_2OF_9$

So far the Sphere Projection method and the Chicken Wire method has been applied to a well-studied molecule, water, and to a molecule that is of current interest, $H_6Si_2O_7$. The next step is to apply the methods to a molecule that is less studied.

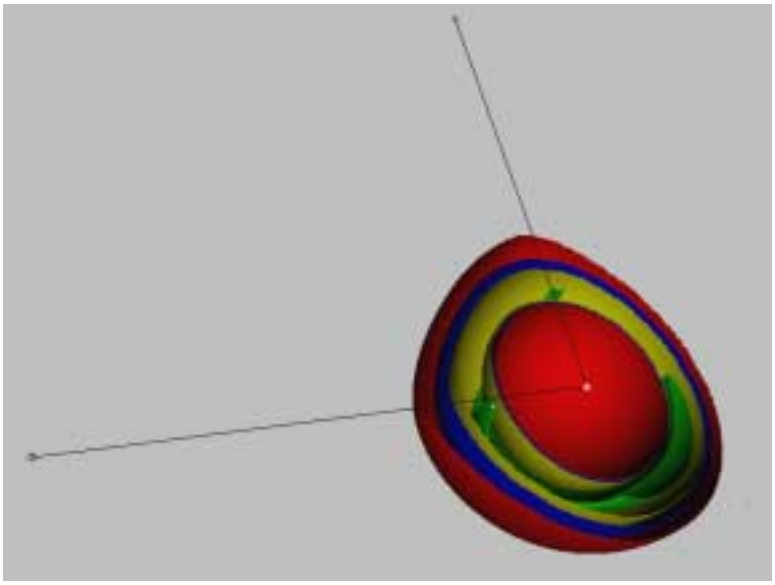

Figure 6.9: 3D representation $-\nabla^2\rho(\mathbf{r})$ of $NaLi_2Si_2OF_9$ sliced through the SiOSi plane.

Gibbs et al completed preliminary studies on low albite. The critical point properties of the VSCCs for the bridging oxide anions were determined. Low albite contains oxide anions that are either bonded to two silicon cations or to a silicon and an aluminum and in some cases to one or two sodium cations. Of the four oxide anions linked to two silicon cations, three are only bonded to two silicon cations and exhibit only one lone pair concentration as found for $H_6Si_2O_7$ and for quartz. The fourth, however, is bonded to two silicon cations and a sodium cation. This oxide anion exhibits two lone pair local concentrations. It was also suggested that the sodium-oxygen bonded interaction may split the lone pair girdle into two closely separated parts [10]. In an effort to verify this statement, the molecule $NaLi_2Si_2OF_9$ was devised and optimized. Regretfully, optimization distorted the molecule in such a way

so that such a conclusion cannot be made. This did not, however, prevent the methods described in this dissertation from being applied.

Figures (6.9) and (6.10) show the three-dimensional representation of the Laplacian isosurfaces of $NaLi_2Si_2OF_9$. The red surfaces are the $-\nabla^2\rho(r) = 0e/\mathring{A}^5$ isosurfaces. The blue are the $-\nabla^2\rho(r) = 5e/\mathring{A}^5$ isosurfaces. The yellow are the $-\nabla^2\rho(r) = 10e/\mathring{A}^5$ isosurfaces. Finally, the green are the $-\nabla^2\rho(r) = 19e/\mathring{A}^5$ isosurfaces. Notice that in these images, the girdle that was found to exist in $H_6Si_2O_7$ is also represented in this molecule. This is a result of the distortion. Because the distance between the oxide anion and the sodium cation is much greater than intended, the molecule behaves as if the sodium did not exist. The molecule behaves exactly as the $H_6Si_2O_7$ and thus the shell structure is extremely similar.

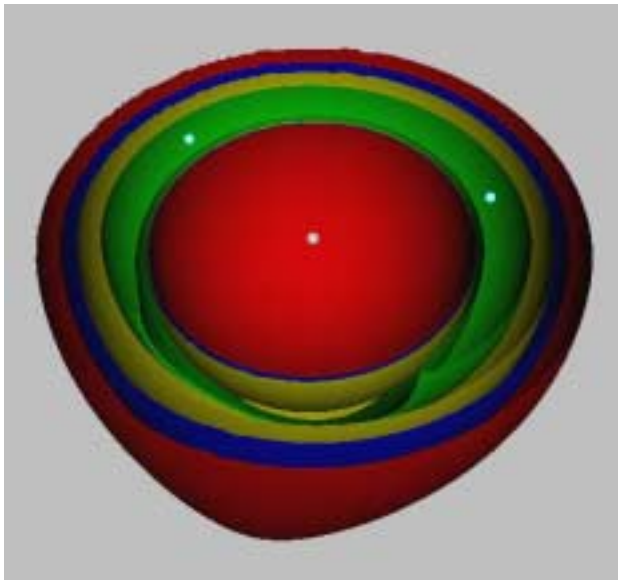

Figure 6.10: 3D representation $-\nabla^2\rho(\mathbf{r})$ of $NaLi_2Si_2OF_9$ sliced through a plane perpendicular to the SiOSi plane.

Chapter 7

Future Work

In the introduction, it was stated that one of the goals of the dissertation topic was to provide many research opportunities. Here are just a few of the pathways for future research that may be pursued.

One of the first projects that will be initiated will be the continued study of low albite. Calculations are now being completed so that the optimization process will not distort the molecule in the manner that was reported here. Researchers with questions of how the sodium cation affects the oxide anion will then have another source with which to seek a solution. Other molecules of interest are surely to follow. With such a variety of structures available, an endless supply of material to be investigated is at hand.

Further studies on the role of the curvature of the Zero Laplacian isosurfaces in the study of molecular models will also be conducted. The applications of the curvature algorithm to the molecular models presented here has shown that curvature of the Zero Laplacian isosurfaces is an interesting topic of study. The shell system of the Laplacian of the electron density function is capable of rendering great information about the crystal itself. Can any of this information be gained from studying the curvature of the Zero Laplacian shells?

A major project that will stem from the research presented here will be a generalization of the Chicken Wire method. The Chicken Wire method has only been applied to molecular models of crystals. The ability to do similar calculations on crystalline structures is also of great interest. Currently, methods to calculate the Laplacian of the electron density function for crystalline structures are being made available. When this is the case, three-dimensional representations of the isosurfaces of the Laplacian will be possible. With the development of such a tool, the electronic properties of crystalline structures may become more visible and much less of a mystery.

Recall that even though each of the applications provided here is mineralogically based, the algorithms and methods were created so that the calculations could be done for any smooth isosurface of a three-dimensional function. The ability of the methods to provide three-dimensional representations for such a wide range of functions opens the door to collaborations with a variety of mathematical fields as well as continued interdisciplinary research. These methods will surely create an opportunity for research connections. With so much emphasis being placed in the literature on visualization and computational representations, such opportunities almost seem endless.

Bibliography

[1] G.A. Arteca and P.G. Mezey. Similarities between the effects of configurational changes and applied electric-fields on the shape of electron-densities. *Theochem-Journal of Molecular Structure*, 88:125–134, 1992.

[2] Neil W. Ashcroft and David Mermin. *Solid State Physics*. Holt, Rinehart, and Winston, New York, NY, 1976.

[3] R.F.W. Bader. "gridv.for". Fortran code, version 81891. Modifications of the original program were completed by M.B. Boisen, R. Downs, and T.A. Keith.

[4] R.F.W. Bader. *Atoms in Molecules*. Oxford Science Publications, Oxford, UK, 1990.

[5] R.F.W. Bader and H. Essén. The characterizations of atomic interactions. *Journal of Chemical Physics*, 80:1943–1960, 1984.

[6] R.F.W. Bader and P.J. MacDougall. Toward a theory of chemical reactivity based on charge density. *Journal of the American Chemical Society*, 107:6788–6795, 1985.

[7] R.F.W. Bader, P.J. MacDougall, and C.D.H. Lau. Bonded and nonbonded charge concentrations and their relation to molecular geometry and reactivity. *Journal of the American Chemical Society*, 106:1594–1605, 1984.

[8] M.B. Boisen, Jr. and G.V. Gibbs. *Mathematical Crystallography: An Introduction to the Mathematical Foundations of Crystallography*. BookCrafters, Inc., New York, NY, 1990.

[9] J.E. Dennis, Jr. and Robert B. Schnabel. *Numerical Methods for Unconstrained Optimization and Nonlinear Equations*. Prentice-Hall, Inc., Englewood Cliffs, New Jersey, 1983.

[10] G.V. Gibbs, M.B. Boisen, Jr., L.L. Beverly, and K.M. Rosso. A duality of properties for earth materials and molecules. *in prep*, 2000.

[11] G.V. Gibbs, M.B. Boisen, Jr., F.C. Hill, O. Tamada, and R.T. Downs. SiO and GeO bonded interactions as inferred from the bond critical point properties of electron density distrubutions. *Physics and Chemistry of Minerals*, 25:574–584, 1998.

[12] G.V. Gibbs, F.C. Hill, and M.B. Boisen, Jr. The SiO bond and electron density distributions. *Physics and Chemistry of Minerals*, 24:167–178, 1997.

[13] G.V. Gibbs, O. Tamada, M.B. Boisen, Jr., and F.C. Hill. Laplacian and bond critical point properties of the electron density distributions of sulfide bonds: A comparison with oxide bonds. *American Mineralogist*, 84:435–446, 1999.

[14] J.B. Hendrickson, D.J. Cram, and G.S. Hammond. *Organic Chemistry.* McGraw-Hill Book Company, New York, NY, 3rd edition, 1970.

[15] Stephen T. Hyde and et al. *The Language of Shape.* Elsevier, Amsterdam, The Netherlands, 1997.

[16] Golden Software Inc. Surfer (win32) version 6.04, February 1997.

[17] P.J. MacDougall. *The Laplacian of the electron charge distribution.* PhD. Dissertation, McMaster University, 1989.

[18] R. McWeeny. *Methods of Molecular Quantum Mechanics.* Academic Press, Inc, San Diego, CA, 1989.

[19] John A. Pople and David L. Beveridge. *Approximate Molecular Orbital Theory.* McGraw-Hill Book Co., New York, NY, 1970.

[20] K.M. Rosso, G.V. Gibbs, and M.B. Boisen, Jr. SiO bonded interactions in coesite: A comparison of crystalline, molecular, and experimental electron density distributions. *Physics and Chemistry of Minerals*, 26:264–272, 1999.

[21] Attila Szabo and Neil S. Ostlund. *Modern Quantum Chemistry: An Introduction to Advanced Electronic Structure Theory.* MacMillan Publishing Co., Inc., New York, NY, 1982.

Vita

Lesa Lynn Beverly was born on March 2, 1966 in Norton, VA to James and Sue McReynolds. She married Chris S. Beverly on Christmas, 1981 and has not doubted her decision to do so even after all these years. She has two wonderful children, Shawn and Ashley, who she adores with all her heart. In the fall of 1987, Lesa and Shawn both started school. Shawn began kindergarten and his momma began taking night classes at Clinch Valley College (now the University of Virginia's College at Wise) in Wise, VA. She decided to pursue a bachelor's degree in mathematics with an education minor with the goal of becoming a secondary education teacher. In the fall of 1990, Lesa became a full-time student and graduated summa cum laude in May of 1994. After much prodding from Lesa's husband, Chris, and Jennifer Wilson (a professor at CVC and a close friend to Lesa), Lesa decided to apply to graduate school at Virginia Polytechnic Institute and State University in Blacksburg, VA and was accepted. She began graduate school in August of 1994. In June, 2000, Shawn graduated from Blacksburg High School and in July, Lesa will finish her doctorate. In August, Lesa and her family will relocate to Tyler, Texas where she will begin an assistant professor's position at the University of Texas in Tyler.